Acta Oceanol. Sin., 2017, Vol. 36, No. 7, P. 15–31
DOI: 10.1007/s13131-017-1079-y
http://www.hyxb.org.cn
E-mail: hyxbe@263.net

A performance evaluation of remotely sensed sea surface salinity products in combination with other surface measurements in reconstructing three-dimensional salinity fields

CHEN Jian[1]*, YOU Xiaobao[1], XIAO Yiguo[1], ZHANG Ren[2], WANG Gongjie[2], BAO Senliang[2]

[1] Beijing Institute of Applied Meteorology, Beijing 100029, China

[2] Institute of Meteorology and Oceanography, PLA University of Science and Technology, Nanjing 211101, China

Received 6 May 2016; accepted 17 January 2017

Abstract

Several remotely sensed sea surface salinity (SSS) retrievals with various resolutions from the soil moisture and ocean salinity (SMOS) and Aquarius/SAC-D missions are applied as inputs for retrieving salinity profiles (S) using multilinear regressions. The performance is evaluated using a total root mean square (RMS) error, different error sources, and the feature resolutions of the retrieved S fields. In the mixed layer of the salinity, the SSS-S regression coefficients are uniformly large. The SSS inputs yield smaller RMS errors in the retrieved S with respect to Argo profiles as their spatial or temporal resolution decreases. The projected SSS errors are dominant, and the retrieved S values are more accurate than those of climatology in the tropics except for the tropical Atlantic, where the regression errors are abnormally large. Below that level, because of the influence of a sea level anomaly, the areas of high-accuracy S values shift to higher latitudes except in the high-latitude southern oceans, where the projected SSS errors are abnormally large. A spectral analysis suggests that the CATDS-0.25° results are much noisier and that the BEC-L4-0.25° results are much smoother than those of the other retrievals. Aquarius-CAP-1° generates the smallest RMS errors, and Aquarius-V2-1° performs well in depicting large-scale phenomena. BEC-L3-0.25°, which has small RMS errors and remarkable mesoscale energy, is the best fit for portraying mesoscale features in the SSS and retrieved S fields. The current priority for retrieving S is to improve the reliability of satellite SSS especially at middle and high latitudes, by developing advanced algorithms, combining both sensors, or weighing between accuracy and resolutions.

Key words: soil moisture and ocean salinity, Aquarius, sea surface salinity, vertical retrieval, feature resolution

Citation: Chen Jian, You Xiaobao, Xiao Yiguo, Zhang Ren, Wang Gongjie, Bao Senliang. 2017. A performance evaluation of remotely sensed sea surface salinity products in combination with other surface measurements in reconstructing three-dimensional salinity fields. Acta Oceanologica Sinica, 36(7): 15–31, doi: 10.1007/s13131-017-1079-y

1 Introduction

Two innovative satellite missions have recently been designed to measure sea surface salinity (SSS) from space: SMOS (soil moisture and ocean salinity) and Aquarius/SAC-D. The SMOS satellite was launched in November 2009 (Kerr et al., 2010) and is the second earth explorer opportunity mission of the European Space Agency (ESA). Its goal is to produce SSS fields with an accuracy of 0.1–0.2 with a spatial resolution of 200 km×200 km every 10 d or with a resolution of 100 km ×100 km every month. The Aquarius/SAC-D mission was launched in June 2011 (Le Vine et al., 2010) and is a joint effort between the National Aeronautics and Space Administration (NASA) and the Argentinian Space Agency CONAE (Comisión Nacional de Actividades Espaciales). It is intended to generate monthly averaged SSS at a spatial resolution of 150 km with an accuracy of 0.2. With their unprecedented large-scale coverage, frequency, and accuracy, the salinity data from these two missions are expected to provide important new insights into oceanographic processes, the hydrological cycle, and climate and greatly expand upon the limited number of past measurements.

The remotely sensed measurements of the sea surface temperature (SST), the sea surface height (SSH), and the SSS provide global high-resolution observations; however, they cannot directly estimate the ocean's internal structures. In contrast, *in situ* observation systems such as Argo can reveal the ocean's interior dynamics but only at large-scale and low-frequency resolution and thus undersample the ocean's thermohaline variability. Consequently, several studies have been devoted to investigating the coupling between sea surface signals and vertical structures in the ocean and extrapolating vertical profiles from satellite measurements, which result in reconstructed fields with both high spatio-temporal resolution and reasonable accuracy. These methodologies include a linear regression (Fox et al., 2002; Guinehut et al., 2004, 2012; Buongiorno Nardelli et al., 2012), a single empirical orthogonal function (EOF) reconstruction (sEOF-R) (Carnes et al., 1994), a bivariate EOF reconstruction (Maes and Behringer, 2000), a multivariate EOF reconstruction (mEOF-R) (Buongiorno Nardelli and Santoleri, 2005), a coupled pattern reconstruction (CPR) (Buongiorno Nardelli and Santoleri, 2004), a gravest empirical mode (GEM) method (Meinen and Watts, 2000; Mitchell et al., 2004), and intelligent methods such as genetic algorithms (GA) (Agarwal et al., 2007) and neural networks (NN) (Ballabrera-Poy et al., 2009; Wu et al., 2012).

The newly available satellite SSS information could be used as

Foundation item: The National Natural Science Foundation of China under contract No. 41276088.
*Corresponding author, E-mail: chenj03@126.com

one of the surface inputs. However, the performance of SSS observations in retrieving vertical temperature and salinity profiles (T/S) has never been evaluated using data from the two recent missions. Many studies have focused on the role of surface measurements in retrieving profiles or on the sensitivity of retrieval methods to surface errors. In these studies, the SSS measurements were obtained only from drifting/moored buoys (Buongiorno Nardelli and Santoleri, 2005), Argo floats (Agarwal et al., 2007; Ballabrera-Poy et al., 2009), or the merging of remotely sensed SST and *in situ* observation-based SSS data (Wu et al., 2012; Buongiorno Nardelli et al., 2012). It should be emphasized that simple/ideal error analysis, such as adding random white noise to the *in situ* surface values that are used as inputs for the vertical reconstruction, appears to be inadequate because the fully independent remotely sensed SSS data from the SMOS or Aquarius missions are contaminated with various types of errors, and there are still many uncertainties about their effective accuracy and geographic error distribution. For example, the SSS errors for the SMOS mission potentially stem from the instrument's observations, brightness temperature (Tb) reconstruction, salinity retrieval, and gridding processing and differ by region (Font et al., 2010; Jordà and Gomis, 2010), which complicates the practical application of SSS data. Even in the prototypal system that was recently developed within MESCLA (Buongiorno Nardelli et al., 2012), the SSS fields that are used as inputs are based on *in situ* observations (Buongiorno Nardelli, 2012). This study makes the first attempt to apply purely remotely sensed SSS observations at the global scale and at different resolutions to retrieval technologies and subsequently evaluates their performance.

2 Overview of SSS products

Global products that cover the period from 2011 to 2012 with at least monthly resolution were selected. Five types of version 2.0 SSS retrievals from the SMOS and Aquarius projects that meet the requirements are shown in Table 1.

Table 1. Summary of the considered SSS retrievals

Product name	Spatial resolution/(°)	Temporal resolution	Input data	Remapping method	Start time
SMOS-CATDS L3	0.25	10 d	L1b	simple averaging	May 2010
	0.50	10 d			
	1.00	10 d			
	0.25	monthly			
	0.50	monthly			
	1.00	monthly			
SMOS-BEC L3	0.25	monthly	0.25° grid binned L2	optimal interpolation	Jan. 2010
SMOS-BEC L4	0.25	monthly	0.25° grid binned L2	singularity analysis	Jan. 2010
Aquarius v2.0 L3	1.00	monthly	L2	simple averaging plus local polynomial smoothing	Sep. 2011
Aquarius v2.0 CAP	1.00	monthly	L2 of CAP algorithm	simple averaging	Sep. 2011

2.1 *SSS processing of SMOS versus Aquarius*

The common processing levels and main differences of the two missions are briefly reviewed below.

2.1.1 *Level 1 processing*

At Level 1 (L1), brightness temperature (K) values are measured. This is performed by measuring microwave emissions from the sea surface and correcting for other natural emission sources and sinks.

The SMOS carries a single payload called the microwave imaging radiometer using aperture synthesis (MIRAS), which is a 2-D interferometric radiometer with multiangular and dual-polarization (or full-polarization) that operates at 1.413 GHz. The 69 antennas in the MIRAS instrument synthesize a full image every 1.2 s from the intercorrelations of the simultaneous antenna measurements. The resulting field of view (FOV) covers a width of approximately 1 000 km at an average spatial resolution of 43 km. Thus, the signals from many small antennas are synthesized to achieve the resolution of a large antenna by observing the same grid point in the FOV at several incidence angles (0°–65°) and polarizations. The Aquarius instrument consists of three radiometers that detect surface emissions to measure the salinity and a scatter meter to simultaneously detect the ocean waves used in the sea surface roughness corrections. The three radiometers measure radiation at vertical and horizontal polarizations at 1.413 GHz and are aligned with a 2.5 m diameter antenna reflector to generate three fixed beams at several angles (28.7°, 37.8°, and 45.6°) to the sea surface. The three beams range in size from 90 to 150 km and form a 390 km wide swath. Thus, the SMOS and Aquarius sensors have different radiometer architectures (e.g., number of receivers; incidence angles), operation principles (e.g., interferometric vs. Dicke radiometer; Stokes parameters measured), swath coverage (≈1 000 km vs. ≈390 km), spatial resolutions (≈40 km vs. ≈100 km), and revisit time (3 d vs. 7 d). As a result, the SMOS resolution is higher than Aquarius', with each location on earth seen by the SMOS under a wide range of incidence angles. On the other hand, Aquarius has a few advantages over the SMOS: its radiometric sensitivity is much better (≈0.12 K over 1.44 s integration time), it has the advanced radio frequency interference (RFI) filtering by using very short time integration subsamples (of the order of 10 ms), it uses a scatterometer to help with the correction of the surface roughness effects, and its beams point towards the night side of the earth to avoid a sun contamination.

Differences also exist in a brightness temperature calibration and correction. Both SMOS and Aquarius use the correlated and uncorrelated noise injection as an internal calibration and use the cold sky as an external calibration. But for Aquarius, additionally, a vicarious calibration is performed using models over the ocean, Antarctica, and Amazon rainforest. After calibration, some corrections are applied to the brightness temperature to obtain the signal from the earth surface and to filter the contributions from celestial bodies (a galaxy, the sun, and the moon). The main difference is that Aquarius brightness temperature is cor-

rected for both direct and reflected celestial contributions while the SMOS brightness temperature is only suffered to reflected corrections.

Besides the contributions of the Faraday rotation, the celestial, the atmosphere, and the brightness temperature bias, the errors related to the radiometric sensitivity are expected to be the most important errors in the L1. The sensitivity of the brightness temperature to the SSS is low and depends on the incidence and the polarization as well as the SST (0.5 K at 20°C and 0.3 K at 5°C). It differs for the two sensors and thus leads to different noise levels in the calibrated brightness temperature. As reported in Pablos et al. (2014), the noise level [standard deviation (STD) divided by mean] of the Aquarius brightness temperature varies from 0.2% to 0.4% over sea while the SMOS brightness temperature noise varies from 1.3% to 2.5%. In addition, the difference between the SMOS brightness temperature and the Aquarius brightness temperature is found to be target dependent. Aquarius is systematically measuring warmer brightness temperature than the SMOS; the difference is higher over land targets (≈5–8 K) and decreases over colder targets (≈3–5 K over ice, ≈0.1–0.3 K over sea). This indicates there may be a nonlinear effect between the two radiometers, and not only a bias (Dinnat et al., 2014).

2.1.2 *Level 2 processing*

At Level 2 (L2), the acquired brightness temperature can be transformed to the SSS. The brightness temperature is related to the seawater's dielectric properties through the dielectric function, and these properties are modulated by the salinity to a certain extent at lower microwave frequencies (e.g., L-band, 1.413 GHz). Thus, the brightness temperature can be expressed as a function of the SSS. A simple least-squares regression can thus minimize the differences between the brightness temperature measurements and its values simulated by the forward model. The forward model considers the target variables, such as SSS, SST, and wind, in addition to the known parameters, which include the incidence and azimuth angles and possibly other roughness descriptors depending on the roughness model that is used. It also requires auxiliary information, including the background SST, wind speed (WS) and/or wind direction (WD), as initial physical constraints.

There are notable differences in the way this retrieval is performed by both missions. First, their forward models use different parameterizations for the dielectric constant. The SMOS uses the dielectric constant model by Klein and Swift (KS). Aquarius uses a more recent model developed by Meissner and Wentz (2012). Second, they use different roughness description information (as well as roughness models). For the SMOS, the information, including the WS and the WD, are taken from the European Centre for Medium-range Weather Forecasts (ECMWF) or the National Centers for Environmental Prediction (NCEP). For Aquarius, in addition to the WS and WD from the NCEP, the integrated scatterometer is used to measure simultaneous oceanic backscatter to improve the roughness correction. Thirdly, they use different ancillary data as input. The reference SSS is the WOA 2009 for the SMOS and the hybrid coordinates ocean model (HYCOM) for Aquarius. Finally, the domain (space, time, reference frame) where the retrieval is performed differ. For the SMOS, the comparison concerns the brightness temperature in the antenna reference frame over a small region of the Pacific Ocean. For Aquarius, the comparison concerns antenna temperatures (i.e., including the Faraday rotation, celestial, atmosphere effects, and antenna pattern) and are performed globally.

At this stage, the errors are generated by the geophysical bias introduced by the forward model and the errors in the auxiliary data. Other geophysical factors that are expected to have an impact on the SSS errors are the sea state (waves and swell), foam, surface currents, or rain. The largest single error source is the sea surface roughness effects caused by wind and waves. As reported in Dinnat et al. (2014), the SMOS dielectric constant model, compared with the Aquarius one, shows improved agreement with the Argo data in the latitude band around approximately –45° and in a few coastal areas, but shows a significant degradation around approximately –60° and for waters colder than 3°C. The differences in their ancillary SSS products could explain biases of up to 0.1, varying in time. It means, regardless of the roughness effects, both missions have their own strengths and weaknesses in retrieval methods depending on latitude, temperature, and time. As for the roughness correction, it has been demonstrated that use of active in addition to passive L-band measurement reduces the root mean square (RMS) error of the SSS by about 40% (Meissner et al., 2014). This gives Aquarius a clear advantage over the SMOS. Retrieval methods also differ for the various SSS products within the same mission, which will be described below.

2.1.3 *Level 3 processing*

At Level 3 (L3), the large amounts of noisy L2 data are used to generate the gridded products. The errors in the measured brightness temperature are estimated to be approximately 1 K, and thus the RMS error for a single SSS retrieval is expected to be greater than 1.0. However, the spatial and temporal resolutions of the SSS data will be quite high. In this stage, the large amount of data obtained by the satellite is synthesized, and a description of the SSS is generated with fields of higher accuracy than the L2 data. Several synthesis methods have been developed for the different SSS products and are described separately for two missions below.

2.2 *SMOS retrievals*

The SMOS SSS retrievals with various resolutions from two data centers are used.

The CATDS/CEC-OS SMOS Level 3 SSS research products (SMOS-CATDS for short) are computed by the Ocean Salinity Expertise Center (CEC-OS) of the CNES-IFREMER Centre Aval de Traitemenent des Donnees SMOS (CATDS) at IFREMER, Plouzane (France) (covering 2010–2012, Version 2.0), and are distributed in NetCDF format (ftp://user:password@eftp.ifremer.fr/salinity). The inputs are the ESA first reprocessing (2010–2011) or operational (2012–present) L1B data. The first Stokes brightness temperatures at the surface level are estimated from those at the XX and YY antenna polarizations (and thus are not affected by Faraday rotation) and are then subjected to incidence angle binning, down sampling, and gridding separately for the ascend/descend passes at 25 km resolution on a daily interval. After being improved by taking into account the instrument errors (calibration) and spatio-temporal variability of the data (geophysical, RFI), the aggregated brightness temperatures can be used to retrieve the SSS. A small slope approximation model is used for the roughness correction (Johnson and Zhang, 1999). The L3 is obtained via a simple average after thorough filtering of inconsistent SSS data (interorbit consistency check) and is based on more consolidated auxiliary data than the ESA L2 data because it has lower operational constraints. Six products with different resolutions are considered: 10 d composites at 0.25°, 0.50°, and 1.00° resolutions and monthly composites at 0.25°, 0.50°, and 1.00° resolutions.

Two of the products are produced monthly on a 0.25° grid at

the SMOS Barcelona Expert Center (SMOS-BEC): the optimally interpolated (L3) and the fused (L4) products (SMOS-BEC L3 and L4 for short). These products are distributed by the SMOS Levels 3 and 4 Production and Distribution Centre (CP34) at the BEC in the NetCDF format (http://cp34-bec.cmima.csic.es). They are computed from the L2 salinity data of the ESA 2012 and 2013 reprocessing campaigns. The quality flags and descriptors in the L2 files allow unreliable SSS values to be discarded using geophysical filters, retrieval filters, and geometrical filters. All of the L2 products developed at the BEC are based on a semiempirical roughness model (Guimbard et al., 2012).

The SMOS-BEC L3 data are produced by optimally interpolating 0.25°×0.25° grid binned L2 SSS data. The monthly WOA 2009 is used as the background field. Validation with near-surface Argo measurements demonstrated that the implementation of the objective analysis significantly improves the accuracy of the data with respect to simply binned maps.

The SMOS-BEC L4 data are obtained with a singularity analysis-based fusion technology (Turiel et al., 2009). A high quality variable, such as SST (T_{SS}), can be used as a template to restore the multifractal structure of the singularity fronts in noisy variables, such as SSS (S_{SS}). It follows the local relationship: S_{SS}= a×T_{SS}+b, where a and b are the local slope and intercept coefficients, respectively. Singularity analysis-based fusion can be used not only to improve the signal level but also to increase the spatial and temporal resolution of the fused maps provided that the SST has the target spatio-temporal resolutions.

Three different roughness models are run in parallel for the SMOS. The first two are theoretical, one of which is used in the SMOS-CATDS (Model 2), while the third one is semiempirical that is used in the SMOS-BEC (Model 3). These models roughly agree on a linear increase of emissivity with the WS for low and medium wind conditions, but well differ in describing the emissivity modification under intense wind conditions. Some studies illustrated that the SSS bias and STD error are much lower for the Model 3 as compared with the Model 2 for winds higher than 12 m/s, and are very similar for both models at the WS below 12 m/s (Guimbard et al., 2012). However, other simple comparisons against *in situ* measurements showed slightly better performance of the SSS retrievals based on the Model 1 than those based on the Models 2 and 3 (Xie et al., 2014).Thus, a more robust validation of different roughness models of the SMOS will be necessary in the future.

2.3 *Aquarius retrievals*

Two monthly Aquarius SSS retrievals on a 1° grid from two data centers are used.

The Aquarius validated (Version 2.0) L3 data (Aquarius V2.0 L3 for short), which are in HDF5 format, are produced by the NASA Goddard Space Flight Center (NASA/GSFC) (ftp://podaac-ftp.jpl.nasa.gov/allData/aquarius/). They are gridded files obtained by remapping L2 orbital SSS data onto a 1° grid, and the values represent the monthly average at each grid cell. For the L2 salinity retrieval, a surface roughness model based on actual post-launch Aquarius observations was developed (Meissner et al., 2012) in which scatterometer cross-section measurements and NCEP WS and WD fields are used together to generate the roughness correction. After the L3 remapping, a local polynomial smoothing method is used to smooth this retrieval.

The Aquarius V2.0 CAP L3 data (Aquarius V2.0 CAP L3 for short), which are in NetCDF format, are produced by the NASA Jet Propulsion Laboratory (NASA/JPL). In the CAP version, to remove the dependence on the NCEP WD as in the standard product, a combined active-passive (CAP) algorithm (Yueh and Chaubell, 2012) is developed to simultaneously retrieve the salinity and the wind. Unlike the standard algorithm which fully uses the NCEP wind for data correction, the CAP algorithm uses the NCEP wind only as a constraint. In addition, the CAP algorithm does not require monthly climatology SSS maps for the salinity retrieval. Besides, this analysis is not subject to the additional smoothing procedure.

The standard and CAP algorithms have their own strengths and weaknesses. However, it has been reported that, in addition to a reduction in the zonally averaged biases, the CAP algorithm improves the RMS error by 13% over the standard version (Reagan et al., 2014) and performs more consistently with the seasonal variation (Yueh et al., 2014) when compared with *in situ* SSS. Thus it can be demonstrated that using the combined passive/active L-band WS from Aquarius instead of NCEP WS leads to a significant improvement in the SSS accuracy.

2.4 *Other products and data pre-processing*

2.4.1 *In situ (-based) and altimeter products*

The *in situ* profiles are taken from the CORA3 data set of the Coriolis data center (http://www.coriolis.eu.org). Only Argo profiles that contain both temperature and salinity (used to calculate a gravitational potential anomaly, i.e., GPA) and that are valid to depths of 1 000 m are selected. These observations are preprocessed according to the Argo recommendations for a data quality control and are interpolated to standard levels. They are then used as training data (2000–2010) to compute the statistics that relate the surface and subsurface fields, as test data to retrieve S, and as independent validation data (from September 2011 to December 2012).

The ARIVO data set is monthly fields defined on a 0.50° Mercator grid from the surface to 2 000 m on 151 vertical levels (http://www.ifremer.fr/lpo/files/isas_globana13/). They are computed using all available *in situ* profiles and an optimal interpolation method for 2004–2010 (delayed time) and 2011–2012 (near-real time). The monthly gridded fields averaged from 2004 to 2010 are used as climatology monthly means to compute the S anomalies. The fields from 2012 are used for comparison with the retrieved S fields in the qualitative analysis.

An altimeter sea level anomaly (SLA) product with daily and 0.25° resolutions was produced by Ssalto/Duacs and distributed by Aviso with support from CNES (http://www.aviso.oceanobs.com/duacs/). The SLA fields are recalculated using the 7 a time mean from 2004 to 2010. The steric components of the SLA are extracted using regression coefficients from a study that compared the *in situ* and altimeter observations (Guinehut et al., 2006). The SLA maps are combined over the SSS composite period (10 d or 1 month) and are remapped on the SSS grids (when necessary) using bilinear interpolation. The SLA data from September 2011 to December 2012 are used for the test.

2.4.2 *Data preprocessing*

To reduce the errors due to salinity stratification, first, only Argo profiles with an uppermost depth less than 5 m were selected. Then, for three standard layers, i.e., 0, 5, and 10 m, three interpolation methods, i.e., cubic polynomial, cubic spline and Akima interpolations, were implemented at the same time. The average of the values from all the three (the first two) methods were taken as the final values for 5 m and 10 m layers (0 m layer); on each layer, if any interpolated value was far from the average more than 5%, the corresponding profile would be removed.

To consider only non-rainy conditions, the Argo profiles were removed if with rain events in a collocation radius of 100 km and 5 d. That is, for one profile, if the rain rates around it within a spatial radius of 100 km and a temporal interval of 5 d were greater than 0.1 mm/h, this profile would be removed.

The *in situ* and satellite observations coincide in time and space in this way. First, if the average time window of a satellite SSS map (e.g., from 1 May to 31 May for a monthly map of May 2011) covered a profile's date (e.g., 7 May), the satellite SSS map and the *in situ* salinity profile would be taken as temporal matchups. Then, for a pair of temporal matchups, the satellite SSS value on the grid (i.e., 0.25°, 0.50°, or 1.00° grids) the closest to the profile's position (e.g., 12.4°N, 117.6°W) was selected as the spatial counterpart of the profile salinity.

This salinity stratification between the first centimeter of the surface layer sampled by satellites and the ~5 m depth sampled by ARGO, as well as this rain effect and spatial/temporal displacement, have been cited as potential sources of error in validation of satellite-based SSS. However, most studies agree that the existing global Argo array provides sufficient data for large-scale validation of SMOS/Aquarius SSS. Drucker and Riser (2014) proved that the errors due to spatial and temporal displacement and the depth of measurement are insignificant for global validation of Aquarius, and errors due to heavy precipitation events contribute less than 0.03 bias in the tropics and 0.025 globally as they occur infrequently, though causing stratification greater than 0.1 during their lasting of approximately 2–8 h. One study on the signature of rainfall on the salinity from SMOS and the salinity from surface drifters measurements of 45 cm below the surface both find the decrease associated with rainfall of approximately –0.2 mm/h, indicating their insignificant discrepancies (Boutin et al., 2014). Other studies demonstrate that rain can only cause scene-averaged salinity offsets that are as large as the accuracy goal for Aquarius of 0.1×10^{-3} (Asher et al., 2014). So, after the preprocessing, we have considered that the Argo measurements are representative of the "real" SSS field. Although this is not strictly true, the assumption is not too strong as to invalidate the results.

3 Methods

3.1 *Method 1: multilinear regression*

The linear regression method used to retrieve vertical profiles was first proposed by Guinehut et al. (2004) using simulated data sets. The method was applied by Larnicol et al. (2006) using real regional observations and by Guinehut et al. (2012) using real global observations and was recently expanded by Buongiorno Nardelli et al. (2012) to integrate SSS products and to increase the effective resolution of the SST products. On the basis of the 3-D thermohaline fields synthesized using this method, a global 3-D geostrophic ocean circulation was estimated using the thermal wind equation (Mulet et al., 2012), and the evolution of a mesoscale cyclonic eddy was described using inviscid, adiabatic, semi-geostrophic diagnostic equations (Buongiorno Nardelli, 2013).

The subsurface salinity at a given position can be estimated using a multiple linear regression:

$$\delta S(z) = \lambda(z)\delta a_{\rm sl} + \theta(z)\delta S_{\rm SS}, \tag{1}$$

where δ denotes anomalies with respect to monthly climatology; λ and θ are regression coefficients of the SLA and the SSS onto the salinity, respectively; and $a_{\rm sl}$ denotes the SLA and $S_{\rm SS}$ is SSS. These parameters vary with depth, location, and time (only depth, z, dependency is shown for clarity) and can be expressed as covariances between the variables:

$$\lambda(z) = \frac{\langle \delta S_{\rm SS}, \delta S_{\rm SS}\rangle \cdot \langle \delta a_{\rm sl}, \delta S(z)\rangle - \langle \delta a_{\rm sl}, \delta S_{\rm SS}\rangle \cdot \langle \delta S_{\rm SS}, \delta S(z)\rangle}{\langle \delta a_{\rm sl}, \delta a_{\rm sl}\rangle \cdot \langle \delta S_{\rm SS}, \delta S_{\rm SS}\rangle - \langle \delta a_{\rm sl}, \delta S_{\rm SS}\rangle^2}, \tag{2}$$

$$\theta(z) = \frac{\langle \delta a_{\rm sl}, \delta a_{\rm sl}\rangle \cdot \langle \delta S_{\rm SS}, \delta S(z)\rangle - \langle \delta a_{\rm sl}, \delta S_{\rm SS}\rangle \cdot \langle \delta a_{\rm sl}, \delta S(z)\rangle}{\langle \delta a_{\rm sl}, \delta a_{\rm sl}\rangle \cdot \langle \delta S_{\rm SS}, \delta S_{\rm SS}\rangle - \langle \delta a_{\rm sl}, \delta S_{\rm SS}\rangle^2}, \tag{3}$$

where <*a*, *b*> is equivalent to *a*′*b*/*n*, and *n* is the number of samples.

The seasonal regression coefficients (λ and θ) are computed on each 1° grid using all of the historical (2000–2010) *in situ* observations in a radius of influence of 5° latitude and 10°–25° longitude to reach a minimum of 500 profiles (Guinehut et al., 2012).

The forecast variance (i.e., signal variance), the regression variance, and the error variance are as follows, respectively:

$$\sigma_{\rm f}^2(z) = \langle \delta S(z), \delta S(z)\rangle, \tag{4}$$

$$\sigma_{\rm r}^2(z) = \lambda(z)\langle \delta a_{\rm sl}, \delta S(z)\rangle + \theta(z)\langle \delta S_{\rm SS}, \delta S(z)\rangle, \tag{5}$$

$$\sigma_{\rm e}^2(z) = \sigma_{\rm f}^2(z) - \sigma_{\rm r}^2(z). \tag{6}$$

The unbiased estimate of the explained variance (EV, i.e., the ratio of the regression variance to the forecast variance) is

$$\begin{aligned} V_{\rm e}(z) &= \hat{R^2}(z) = \hat{\sigma_{\rm r}^2}(z)/\hat{\sigma_{\rm f}^2}(z) \\ &= 1 - [(n-1)/(n-r-1)][1 - \sigma_{\rm r}^2(z)/\sigma_{\rm f}^2(z)], \end{aligned} \tag{7}$$

where $V_{\rm e}$ is the EV; and r is the number of regression variables and is equal to 2 here.

3.2 *Method 2: multivariate EOF reconstruction*

The mEOF-R technology was proposed by Buongiorno Nardelli and Santoleri (2005) and applied by Buongiorno Nardelli et al. (2012) to create a high-resolution observation-based product. It is based on the multivariate EOF analysis of the vertical profiles of temperature, salinity, and gravitational potential (P) (i.e., T, S, $P_{\rm g}$) and on the assumption that only a few modes are needed to explain most of the variance/covariance of the fields.

First, a $3m\times n$ multivariate observation matrix $\boldsymbol{X}$ is constructed from the temperature, salinity and P data sets, which are all of $m\times n$ dimensions, and where n is the profile number, and m is the vertical level number. The data are normalized by dividing each parameter by its STD across the entire profile, and the mean profiles are preliminarily subtracted to obtain the anomalies. The columns of this matrix consist of the three normalized temperature, salinity and P anomalies, which are each taken at the same location.

$$\boldsymbol{X} = \begin{bmatrix} T(0,t_1) & T(0,t_2) & \cdots & T(0,t_n) \\ \vdots & \vdots & & \vdots \\ T(z_m,t_1) & T(z_m,t_2) & \cdots & T(z_m,t_n) \\ S(0,t_1) & S(0,t_2) & \cdots & S(0,t_n) \\ \vdots & \vdots & & \vdots \\ S(z_m,t_1) & S(z_m,t_2) & \cdots & S(z_m,t_n) \\ P_g(0,t_1) & P_g(0,t_2) & \cdots & P_g(0,t_n) \\ \vdots & \vdots & & \vdots \\ P_g(z_m,t_1) & P_g(z_m,t_2) & \cdots & P_g(z_m,t_n) \end{bmatrix}. \tag{8}$$

Singular value decomposition (SVD) is then performed on the 3 $m\times n$ multivariate observation matrix to identify several (N)

multicoupled modes, each of which contains three patterns (L_k, M_k, N_k) that correspond to the three parameters being considered. The T, S and P can thus be expanded in terms of the three series of patterns with the same amplitude (a_k) for all parameters:

$$\left.\begin{aligned} T(z,t) &= \sum_{k=1}^{N} a_k(t) L_k(z) \\ S(z,t) &= \sum_{k=1}^{N} a_k(t) M_k(z) \\ P_g(z,t) &= \sum_{k=1}^{N} a_k(t) N_k(z) \end{aligned}\right\}. \tag{9}$$

Here, the construction of the $3m\times n$ multivariate observation matrix and the implementation of the SVD are performed using historical (2000–2010) *in situ* observations. The modes (L_k, M_k, N_k) are identified for each 1° grid using all of the observations in an radius of influence that is the same to that used for the regression coefficients of Method 1.

Buongiorno Nardelli et al. (2012) show that mEOF-R provides the smallest RMS errors when only two modes are considered. Thus, with these expansions limited to the first two modes, the salinity can be estimated from the surface salinity and from the gravitational potential values ($z = 0$) by solving the system for a_1 and a_2 and substituting them into the truncated expansions:

$$\left.\begin{aligned} a_1(t)M_1(0) + a_2(t)M_2(0) &= S(0,t) \\ a_1(t)N_1(0) + a_2(t)N_2(0) &= P_g(0,t) \end{aligned}\right\}. \tag{10}$$

The univariate/bivariate EOF reconstructions (Carnes et al., 1994; Maes and Behringer, 2000) have a similar theoretical basis and are thus not discussed here.

3.3 *Method 3: self-organizing map*

The self-organizing map (SOM) NN was used by Telszewski et al. (2009) to estimate the monthly partial pressure of carbon dioxide distribution in the North Atlantic from three biogeochemical parameters and was then applied by Wu et al. (2012) to estimate the subsurface temperature in the North Atlantic from remotely sensed SST, SSS, and SSH.

Following their strategies, the SOM maps were first trained using the SST, SSS, and SSH data from historical *in situ* Argo data sets and were then labeled with the subsurface salinity data from these Argo data sets. Finally, they were used to estimate the salinity at several depths from the independent sea surface data.

The SOM map was trained separately in each box area of 15°×15°. Using a hexagon topology function and a Gaussian neighborhood function, each map consists of 25 (5×5) to 289 (17×17) neurons based on the number of historical (2000–2010) profiles within the subarea to reach an average number of 30 samples for each neuron. Before training, each parameter with the monthly mean removed was normalized by its STD to avoid the discrepancy in magnitudes. Each neuron has three components that represent all of the combinations of input variables (SST, SSS, SSH). The relationship between three training parameters, with similar patterns mapped to neighboring regions and dissimilar patterns mapped to separate locations, was the foundation for the labeling and estimation processes.

For each layer, the Argo salinity value at that depth was used to label the trained neural network. On the basis of the SST, the SSS, and the SSH, the salinity values were labeled onto the nearest neurons based on Euclidean distance. For the neurons that are labeled by more than one salinity value, the average salinity value was used as the final labeling value.

The salinity was estimated using the labeled SOM map and sea surface information. Input vectors of the arbitrary position and time had one neuron in the labeled SOM map according to the Euclidean distance; the S value of that neuron became the estimate of the input vectors.

3.4 *Evaluation schemes*

For Method 1, first, using the available global descriptions of the statistical relationships between the surface and subsurface fields, independent (September 2011 to December 2012) *in situ* or collocated satellite surface values are used as inputs to retrieve the salinity values. The types of salinity profiles considered are described in Table 2.

The retrieved profiles are then compared with the validation profiles to compute the RMS errors. This comparison is performed in predetermined areas or in each 15°×15° box. The resulting types of the RMS errors (e_{rms}) are described in Table 3. Some of the RMS errors could be alternately expressed as percentages of the signal STD (p_{situ}, p_{sate}) or of the total RMS error (p_{regr}, p_{satS}, p_{satH}, p_{satSH}) as shown in Table 4. The former denotes the error relative to the signal STD, while the latter denotes the importance of the different sources of error to the total error.

Finally, σ_{satSH} can be associated with the regression coefficients (analogous for σ_{satS} and σ_{satH}, which are not given) as:

$$\begin{aligned} \sigma_{\mathrm{satSH}}(z) &= E\left[(S_{\mathrm{sate}} - S_{\mathrm{situ}})^2\right]^{1/2} \\ &= E\left\{\left[\lambda(z)\cdot(\delta a_{\mathrm{sl}} + \sigma_{\mathrm{SLA}}) + \theta(z)\cdot(\delta S_{\mathrm{SS}} + \sigma_{\mathrm{SSS}}) - \right.\right. \\ &\quad \left.\left. \lambda(z)\cdot\delta a_{\mathrm{sl}} - \theta(z)\cdot\delta S_{\mathrm{SS}}\right]^2\right\}^{1/2} \\ &= E\left\{\left[\lambda(z)\cdot\sigma_{\mathrm{SLA}} + \theta(z)\cdot\sigma_{\mathrm{SSS}}\right]^2\right\}^{1/2}, \end{aligned} \tag{11}$$

where σ_{SLA} and σ_{SSS} are the errors in the satellite SLA and satellite SSS, respectively.

For Methods 2 and 3, only the estimations from the pure *in situ* surface inputs (*in situ* GPA and SSS for Method 2; *in situ* GPA, SSS, and SST for Method 3) or pure satellite surface inputs (satellite SLA and SSS for Method 2; satellite SLA, SSS, and SST for Method 3), such as S_{situ} and S_{sate}, are considered. The corresponding RMS errors include σ_{situ}, p_{situ}, σ_{sate} and p_{sate}.

Table 2. Salinity profile notations

Notation	Classification	Inputs
S_{vali}	validation *in situ* salinity	
S_{clim}	ARIVO climatology salinity	
S_{situ}	retrieved salinity from surface	*in situ* GPA and *in situ* SSS
S_{satS}	retrieved salinity from surface	*in situ* GPA and satellite SSS
S_{satH}	retrieved salinity from surface	satellite SLA and *in situ* SSS
S_{sate}	retrieved salinity from surface	satellite SLA and satellite SSS

Table 3. RMS notations

Notation	e_{rms}, S_1-S_2		Short name	Full name
	S_1	S_2		
σ_{clim}	S_{clim}	S_{vali}	signal STD	
σ_{sate}	S_{sate}	S_{vali}	total error	total error using satellite surface values
σ_{situ}	S_{situ}	S_{vali}	regression error	error caused by the regression model (also error using *in situ* surface values)
σ_{satS}	S_{satS}	S_{situ}	SSS-induced error	error caused by inaccuracies in satellite SSS
σ_{satH}	S_{satH}	S_{situ}	SLA-induced error	error caused by inaccuracies in satellite SLA
σ_{satSH}	S_{sate}	S_{situ}	satellite-induced error	error caused by inaccuracies in satellite values

Table 4. Ratio notations

Notation	Ratio, σ_1/σ_2		Meaning
	σ_1	σ_2	
p_{sate}	σ_{sate}	σ_{clim}	total error using satellite inputs relative to the signal STD
p_{situ}	σ_{situ}	σ_{clim}	error using *in situ* inputs relative to the signal STD
p_{regr}	σ_{situ}	σ_{sate}	weight of regression error in the total error
p_{satS}	σ_{satS}	σ_{sate}	weight of SSS-induced error in the total error
p_{satH}	σ_{satH}	σ_{sate}	weight of GPA-induced error in the total error
p_{satSH}	σ_{satSH}	σ_{sate}	weight of satellite-induced error in the total error

4 Results

4.1 *Comparison among three methods*

As shown in Fig. 1, at the global scale, the performance of the three methods of salinity extrapolation is all improved with respect to climate-based values when using the pure *in situ* (error-free) surface data. The multilinear regression performs best, followed by the mEOF-R, and the SOM performs worst. The latter two technologies take advantage not only of the altimeter and SSS measurements but also of SST (which is not the case for the multilinear regression); however, the adequate training samples (Argo profiles containing both temperature and salinity and valid to a depth of 1 000 m) required for the empirical mode decomposition in the mEOF-R or the feature classification in the SOM are not available. This potentially leads to their poor performance in S extrapolation.

However, when estimating salinity from satellite surface values that contain errors, the mEOF-R method leads to larger RMS errors than the climatology STD at all depths and seems to be much more risky to apply. In contrast, the SOM is much less susceptible to the surface noise and leads to the RMS errors that are equivalent to the climatology STD. The multilinear regression is moderately sensitive to the surface noise, which leads to larger (smaller) RMS errors than the climatology STD above (below) depths of 200 m.

Considering its good performance using noise-free surface values and its moderate susceptibility to the surface noise, the multilinear regression is selected to evaluate the performance of various remotely sensed SSS retrievals in reconstructing 3-D salinity fields.

4.2 *Total error using various SSS inputs*

The profiles that denote the total errors (σ_{situ}, σ_{sate}, p_{situ}, p_{sate}) for several basins using Method 1 are shown in Fig. 2.

At the global scale, the use of *in situ* SSS inputs reduces the RMS differences of salinity by 100% at the surface to approximately 10% at depth (p_{situ}); in contrast, the use of satellite SSS inputs, due to their large errors of 0.25–0.4, cannot improve the S estimates for any of the retrievals (p_{sate}). The four 1.00° retrievals (Aquarius-CAP, CATDS-1° Mon/10d, Aquarius-V2) lead to smaller values of p_{sate} than the four 0.25° retrievals (BEC-L3, BEC-L4,

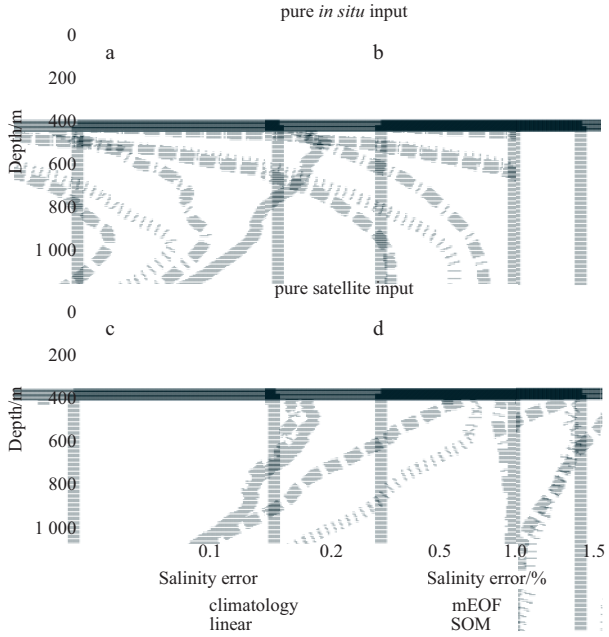

Fig. 1. The profiles of σ_{clim}, σ_{situ} (a) and p_{situ} (b), and the profiles of σ_{clim}, σ_{sate} (c) and p_{sate} (d). Errors are calculated for the three methods (dashed- linear, dotted- mEOF, dash-dotted- SOM) and the global ocean (60°S–60°N, 0°E–360°E). The satellite SSS data used to calculate σ_{sate} and p_{sate} are from BEC-L3.

CATDS-0.25° Mon/10d); the two 0.50° retrievals (CATDS-0.50° Mon/10d) falls between those values. For the three pairs of CATDS retrievals with the same spatial resolution (CATDS-1.00° Mon/10d, CATDS-0.50° Mon/10d, CATDS-0.25° Mon/10d), the ten-day composites yield to moderately larger errors in contrast to the monthly ones. However, it is still the spatial resolutions that generally determine the order of error magnitude. In the tropical Pacific, σ_{sate} is slightly less than σ_{clim} in the upper approximately 100 m layer in all of the retrievals except CATD-0.25°; below 100 m, σ_{sate} is similar to σ_{clim} except in the layer between 300 and 600 m, where σ_{sate} is approximately 10% less than σ_{clim}. This

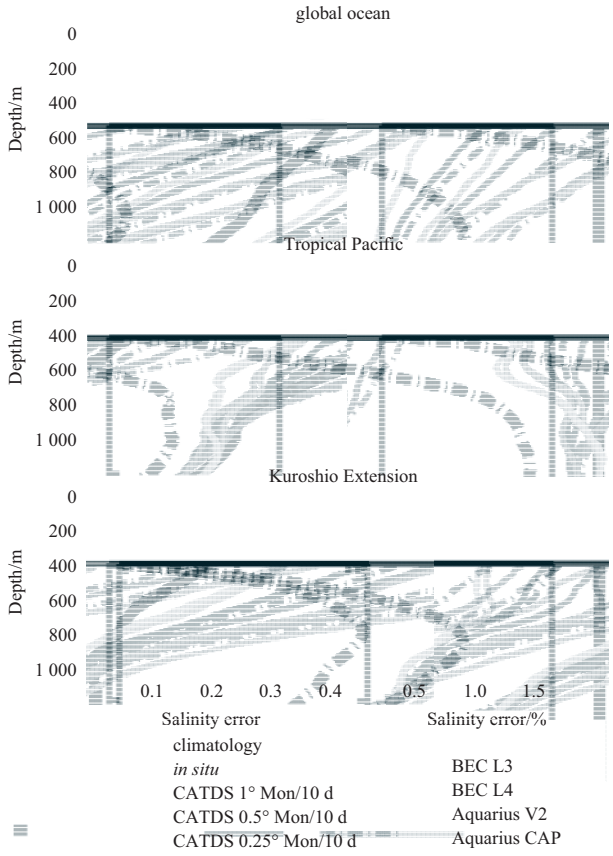

Fig. 2. The profiles of σ_{clim} (thick solid), σ_{situ} (thick dash-dotted), and σ_{sate} (thin) (left) and profiles of p_{situ} (thick dash-dotted) and p_{sate} (thin) (right) for three basins: the global ocean (60°S–60°N, 0°–360°E; top), the tropical Pacific Ocean (30°S–30°N, 120°E–70°W; middle), and the Kuroshio Extension region (30°–45°N, 150°E–150°W; bottom). Method 1 was used for the retrieving salinity. The satellite SSS data used are from all the ten retrievals.

suggests that the spatial and temporal resolutions directly influence the accuracy of the SSS inputs and the retrieved salinity in the upper layer; in contrast, the satellite SSS observations play an insignificant role below that layer. This phenomenon is more evident in the mid-latitude Kuroshio Extension (KE) region, where σ_{sate} in the upper layer is greater than σ_{clim} overall and increases as the spatial resolution increases. In contrast, σ_{sate} in the interior ocean is independent of σ_{SSS} in several SSS retrievals. A comparison of the three basins indicates that the remotely sensed SSS inputs can only improve the salinity estimates in the tropics; in the mid-latitudes, the SSS inputs cannot be used with confidence. Considering the STD error between satellite (e.g., Aquarius L2) and Argo SSS ranging from ~0.3 in the tropics to ~0.7 at high latitudes (Drucker and Riser, 2014), it can be roughly inferred that whether the salinity can be improved mostly depends on whether the SSS itself has reasonable accuracy. This will be discussed in detail in Section 4.3 that distinguishes errors due to surface values from those due to regression methods. The other two pairs of retrievals with the same spatial resolution are also compared. Globally, BEC-L3 performs better than BEC-L4, and Aquarius-CAP performs better than Aquarius-V2.

The non-smoothed version of the Aquarius-V2 was used in an additional test (not shown) and resulted in even larger σ_{sate} values than the smoothed version in all three basins. This implies that the smaller error in Aquarius-CAP is attributable to the CAP algorithm rather than the lack of smoothing.

Although climatology does a better job in representing the vertical structure of the salinity fields at the global scale than the estimates from the satellite SSS measurements, the estimated fields perform better in certain areas or at certain depths, as illustrated in Fig. 2. This needs to be investigated further because the results will help to assess the current capabilities to retrieve 3-D salinity fields using available remotely sensed surface inputs. When these measurements become continuous and reliable in the future, they will also help to address associated questions about remotely sensed SSS observations.

The global p_{sate} maps for all six CATDS retrievals are shown in Fig. 3. Generally, the CATDS SSS inputs yield increasingly smaller S errors as the spatial and temporal resolutions decrease. The differences between the high-resolution and low-resolution maps gradually disappear as the depth increases. Characteristics of the individual levels include the following:

(1) At the surface and at 50-m depth, p_{sate} is less than 1 only in the tropical oceans. In detail, the CATDS-0.25° SSS input performs worse than climatology over most of the global ocean; in contrast, the CATDS-1.00° SSS input performs better throughout the tropical oceans, although to a much smaller extent in the tropical Atlantic Ocean.

(2) At 150 m depth, the regions of p_{sate}<1 expand to the extratropics, excluding the high-latitude southern oceans.

(3) At 300 m depth, the regions of $p_{sate} \geqslant 1$ prevail along the narrow equatorial bands in the ocean interior.

(4) At 500 m depth, the regions of p_{sate}\geqslant 1 gradually change shape and are concentrated around the northwest Pacific Ocean, the southwestern tropical Pacific Ocean, the North and South Atlantic Oceans, and the Indian Ocean.

(5) At 1 000 m depth, p_{sate} is decreased globally and particularly in the North Atlantic Ocean.

Characteristics that are common to all levels include the following:

(1) In the regions south of 45°S, p_{sate} is always greater than or equal to 1;

(2) For most areas, p_{sate} remains above 0.8, indicating that the use of SSS inputs decreases the RMS differences of salinity by less than 20%.

The global p_{sate} maps for the other four retrievals are shown in Fig. 4. On the surface and at 50 m in the tropics, the areas with p_{sate}<1 in the Aquarius retrievals are slightly broader than those in the BEC retrievals. This is expected because the former has a lower spatial resolution (1.00°) than the latter (0.25°). Below that, the differences between the retrievals gradually decrease as the depth increases. Together, Figs 2, 3, and 4 show that the Aquarius SSS inputs generally perform best in terms of the RMS errors for the retrieved salinity. However, the BEC SSS input at a resolution of 0.25° can reach an accuracy that is roughly equivalent to those of the CATDS and Aquarius SSS inputs at resolutions of 1.00°, in particular in the upper tropical ocean; this indicates that processing the BEC SSS may be advantageous to processing the CATDS SSS.

4.3 *Error sources*

The errors in vertically retrieving S can originate from either the regression method or the surface values, both of which are related to the vertical regression coefficients. Figure 5 shows the regression coefficients between the SSS and the salinity (i.e., θ) and between the SLA and the salinity (i.e., λ), which directly determ-

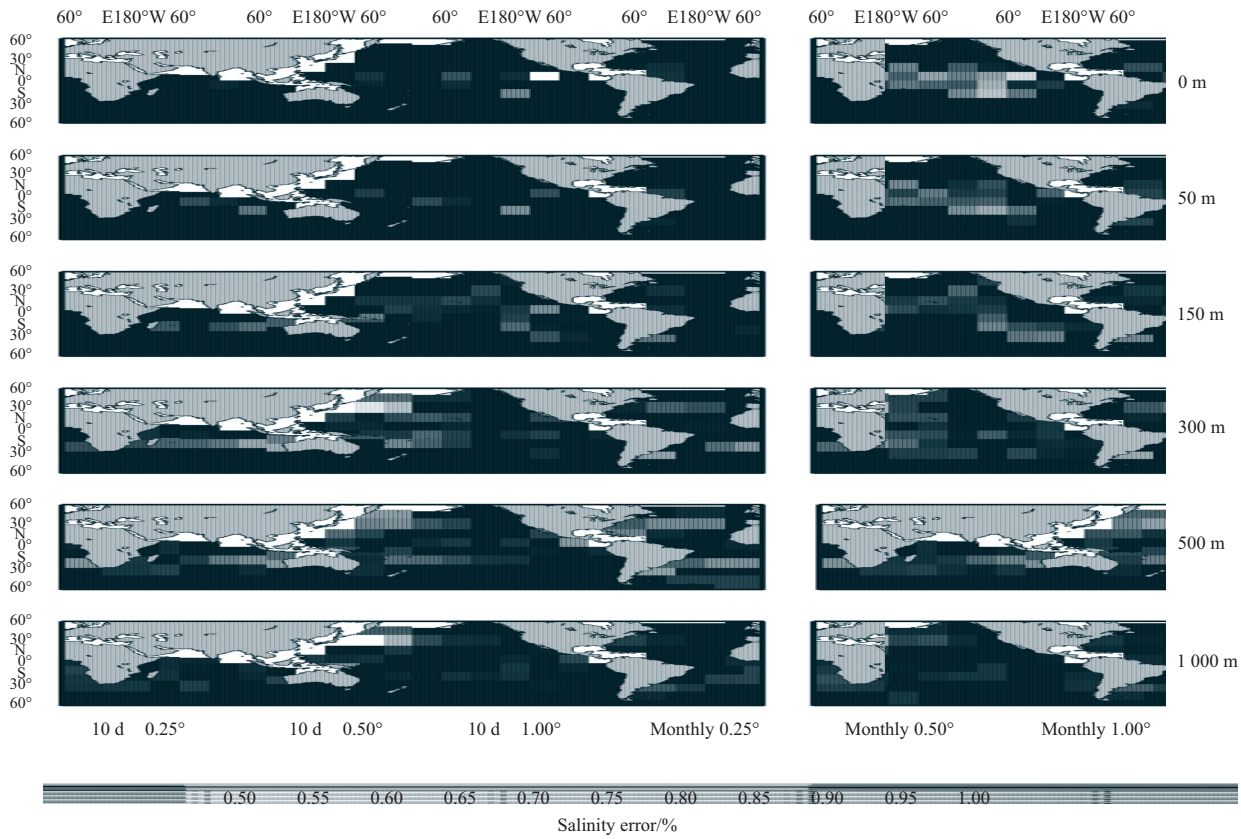

Fig. 3. Maps of p_{sate} at depths of 0, 50, 150, 300, 500, and 1 000 m (from top to bottom). The SSS data are from CATDS products of ten-day composites with resolutions of 0.25°, 0.50°, and 1.00° and monthly composites with resolutions of 0.25°, 0.50°, and 1.00° (from left to right). The values are computed in 15°×15° box. This figure illustrates how the spatial and temporal resolutions of SSS influence the estimated salinity values.

ine the way that the SSS/SLA signals and errors are projected to depth, as well as the EV, which reflects the synthetic effects of the regression.

(1) In the upper layer, θ has uniformly high values at all latitudes. This explains why σ_{sate} is sensitive to the SSS resolution in that layer (Fig. 2) and why the p_{sate} values at 50 m reflect the surface structures (Figs 3 and 4). Below that level, most of the θ values are near 0 except for a vertical zone of high θ values that extends to depths of 400–800 m in the southern oceans; this indicates that the SSS errors in that region remain influential at depth. This accounts for the gradually disappearing surface p_{sate} patterns below 150 m and the large p_{sate} values in the deep oceans south of 45° S, where large SSS errors are projected (Figs 3 and 4).

(2) The tropics are dominated by negative values of λ from the surface to approximately 100 m and by positive values below that level. The maximum positive values are concentrated between 100 and 300 m. At higher latitudes, the North Atlantic and North Pacific Oceans show striking negative and positive regions, respectively, and the South Indian Ocean and South Atlantic Ocean each shows a clear negative region from near the surface to depth. These features account for the displacement of areas of low p_{sate} to middle and high latitudes below 150 m (Figs 3 and 4).

(3) The EV is the greatest in the mixed layer of the salinity ("mixed layer" for short afterwards) at all latitudes where θ is uniformly high and is moderately great from the base of the mixed layer to the deep oceans at higher latitudes, where λ is high or vertical high-θ regions are present. From 100 to 300 m in the tropics, in locations where λ is also high, the EV is smaller due to the strong salinity variations (i.e., forecast variance σ_f^2) because $V_e \approx \sigma_r^2/\sigma_f^2$. This is consistent with the slightly smaller values of σ_{sate} than σ_{clim} in that layer (Fig. 2).

The analysis then focused on the respective importance of the different error sources, which are denoted as σ_{situ}, σ_{satS}, σ_{satH}, and σ_{satSH} (Figs 6 and 7) or p_{regr}, p_{satS}, p_{satH}, and p_{satSH} (Figs 6 and 8). The differences between the results of these retrievals are small (not shown), so only the satellite surface data from the BEC-L3 is shown as an example.

Figure 6 shows the profiles of all of the errors. The weights of the SSS-induced errors decrease from 100% on the surface to approximately 10%–20% at depth (p_{satS}). In contrast, the weights of the SLA-induced errors increase from 0% on the surface to the maximum in the interior oceans (p_{satH}). The level with p_{satS}=p_{satH} is slightly shallower in the tropics than at the mid-latitudes, and the profile of p_{satSH} is roughly parallel to that of p_{satS} (p_{satH}) above (below) this level. The profile of p_{regr} is roughly symmetrical to that of p_{satSH}, which indicates that the regression error (satellite-induced error) is more important in the upper (deep) ocean. However, the importance of each error differs based on the areas and depths.

Figures 7 and 8 show the maps of the absolute and ratio errors, respectively.

(1) On the surface, there is no regression error (p_{regr}=0) and only the SSS-induced error (p_{satS}=1). At 50 m depth, the SSS-induced error is still dominant (p_{satS}>0.5), although the regression error is not insignificant in the tropics (Fig. 8). In detail, σ_{satS} (σ_{situ}) is smaller (larger) in the tropics than in the extratropics

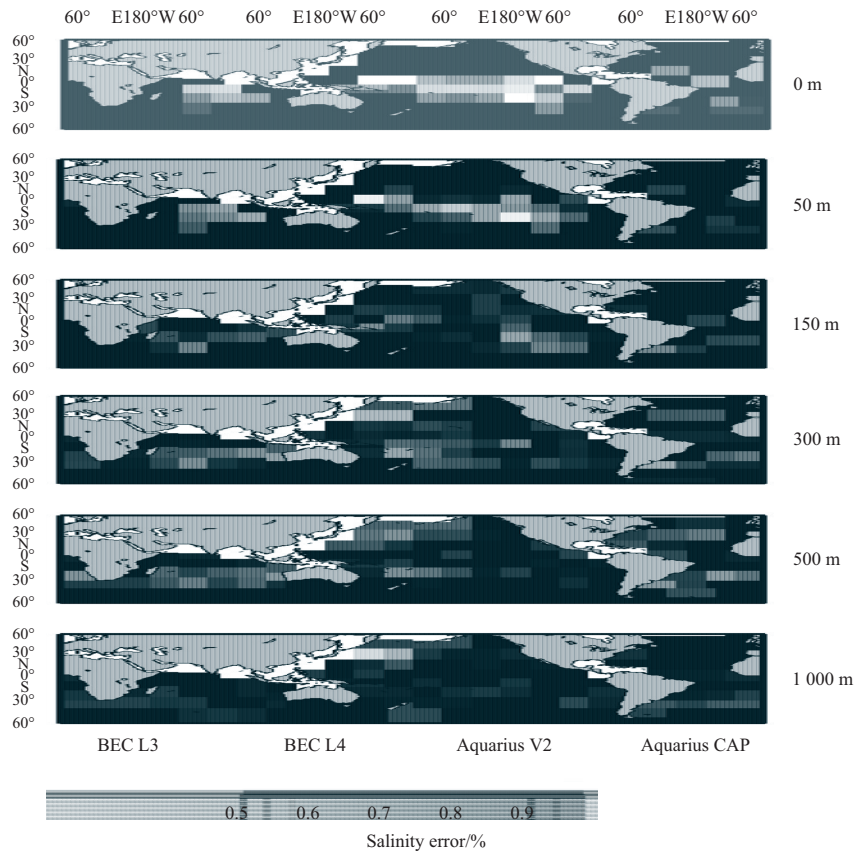

Fig. 4. Maps of p_{sate} at depths of 0, 50, 150, 300, 500, and 1 000 m (from top to bottom). The SSS data used are from monthly BEC-L3, BEC-L4, Aquarius-V2, and Aquarius-CAP products (from left to right). This figure illustrates the differences in the salinity estimated by the different SSS retrievals.

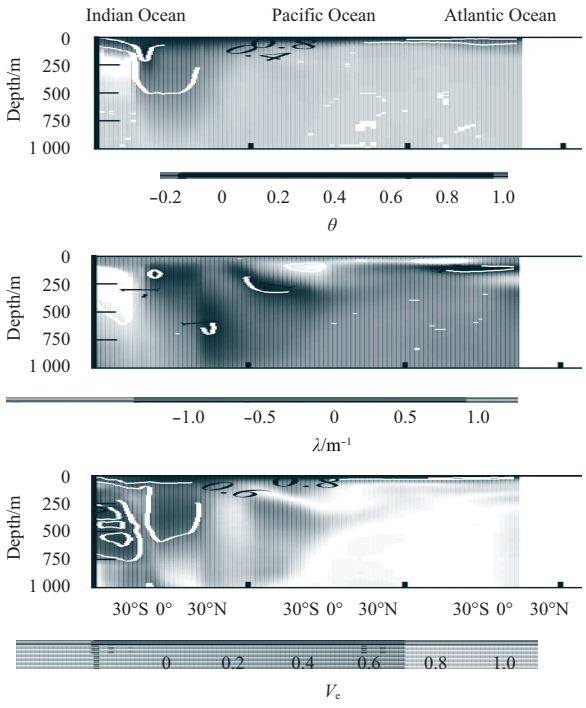

Fig. 5. Depth-latitude sections of annual θ (top row), λ (middle row), and V_e (bottom row) along 70°E in the Indian Ocean, 160°W in the Pacific Ocean, and 30°W in the Atlantic Ocean (from left to right).

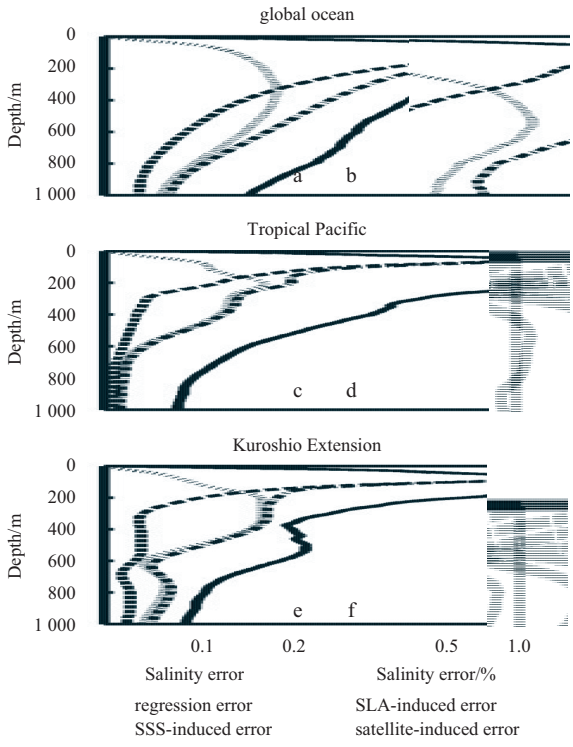

Fig. 6. The profiles of σ_{situ} (a), σ_{satS} (c), σ_{satH} (e), and the profiles of p_{regr} (b), p_{satS} (d), p_{satH} (f), for the three basins shown in Fig. 2. The SSS data used are from the BEC-L3.

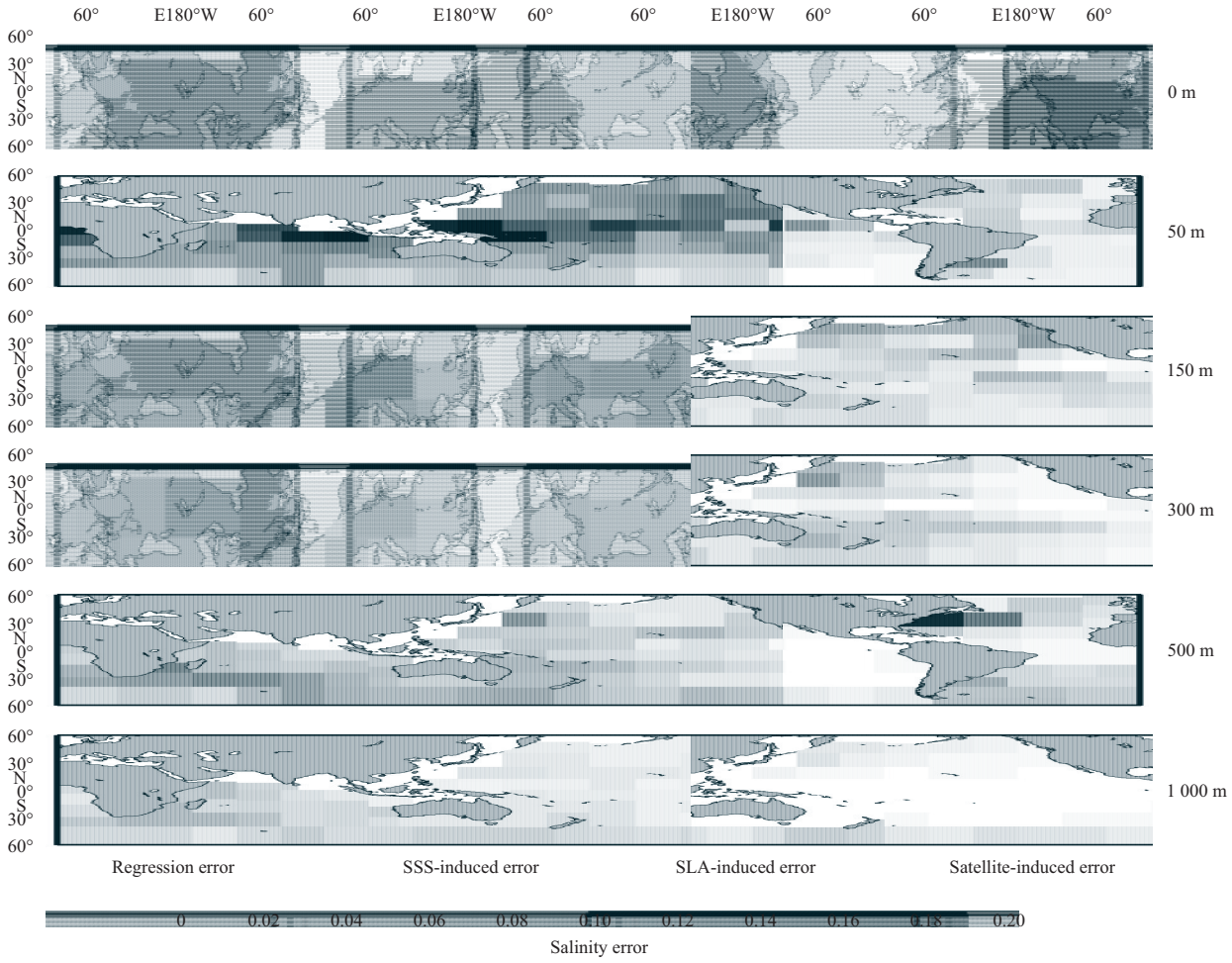

Fig. 7. Maps of σ_{situ}, σ_{satS}, σ_{satH}, and σ_{satSH} (from left to right) at depths of 0, 50, 150, 300, 500, and 1 000 m (from top to bottom). The SSS data used are from BEC-L3.

(Fig. 7). As a result, p_{satS} (p_{regr}) is smaller (larger) in the tropics than in the extratropics (Fig. 8); on the other hand, as a final offset, p_{sate}<1 (p_{sate}>1) in the tropics (extratropics) (Figs 3 and 4). However, the tropical Atlantic Ocean is an exception, with p_{satS}<0.5 (Fig. 8) and p_{sate}>1 (i.e., σ_{sate}>σ_{clim}; Figs 3 and 4). The large values of σ_{sate} (σ_{situ}+σ_{satS}) in that region are induced by the abnormally large values of σ_{situ} rather than σ_{satS} because σ_{satS} is even smaller than in the other tropical oceans. At these two levels, p_{satSH} is almost identical to p_{satS}.

(2) At 150 m, σ_{satSH} is significantly reduced because the impact of SSS becomes insignificant, while the SLA plays an increasingly important role. In contrast, σ_{situ} remains high in the tropics (Fig. 7). As a result, the tropics are dominated by the regression errors instead (p_{regr}>0.5) (Fig. 8). At 300 and 500 m, σ_{satSH} is reshaped by the effects of σ_{satH} and σ_{satS} (Fig. 7). North of 45°S, the regions of p_{satSH}>0.5 (Fig. 8) are roughly consistent with those of p_{sate}<1 (Figs 2 and 3), where the relatively high λ values improve the salinity estimates (Fig. 5). South of 45° S, the regions of p_{satSH}>0.5 (Fig. 8) are consistent with those of p_{sate}>1 (Figs 2 and 3), where the area of large θ values projects below the area of abnormally high σ_{SSS} (Fig. 5). The regions with p_{satSH}>0.5 shrink further down to 1 000 m, and small p_{satSH} values eventually occupy regions such as the Northeast Atlantic Ocean and the southwestern Tropical Pacific Ocean (Fig. 8).

4.4 *Feature resolutions*

Feature resolution issues affect several areas with large salinity differences, including the western Tropical Pacific and regions near the coast, where the SSS gradients are generally strong, and the Northwest Pacific, where considerable mesoscale variability occurs and where the SSS measurements tend to be relatively noisy. It begins with qualitatively examining the salinity patterns on the surface and at a depth of 100 m (Figs 9–12). The 100 m level can be used to differentiate the characteristics of the upper ocean at different latitudes because the depth of the mixed layer varies from 20 to 70 m in the Equatorial Pacific (Delcroix et al., 1996; Ando and McPhaden, 1997), while it is fairly deep and even exceeds 200 m during several months in the Northwest Pacific (Ohno et al., 2004).

Figure 9 shows the salinity fields in the western Tropical Pacific (WTP). On the surface, the CATDS-0.25° SSS field shows extensive small-scale structures. In contrast, the other SSS fields have uniform and smooth patterns; for example, the western Pacific salinity front (WPSF) is clearly marked by the 34.8 isohaline (bold white lines). The BEC-L4 SSS field has a nearly identical but attenuated appearance. For example, the negative anomalies in the northwest and positive anomalies in the southeast both have decreased amplitudes. Compared with the Aquarius-V2 SSS field, the Aquarius-CAP field has somewhat sharper gradients throughout the basin. At 100 m, the salinity fields estimated from

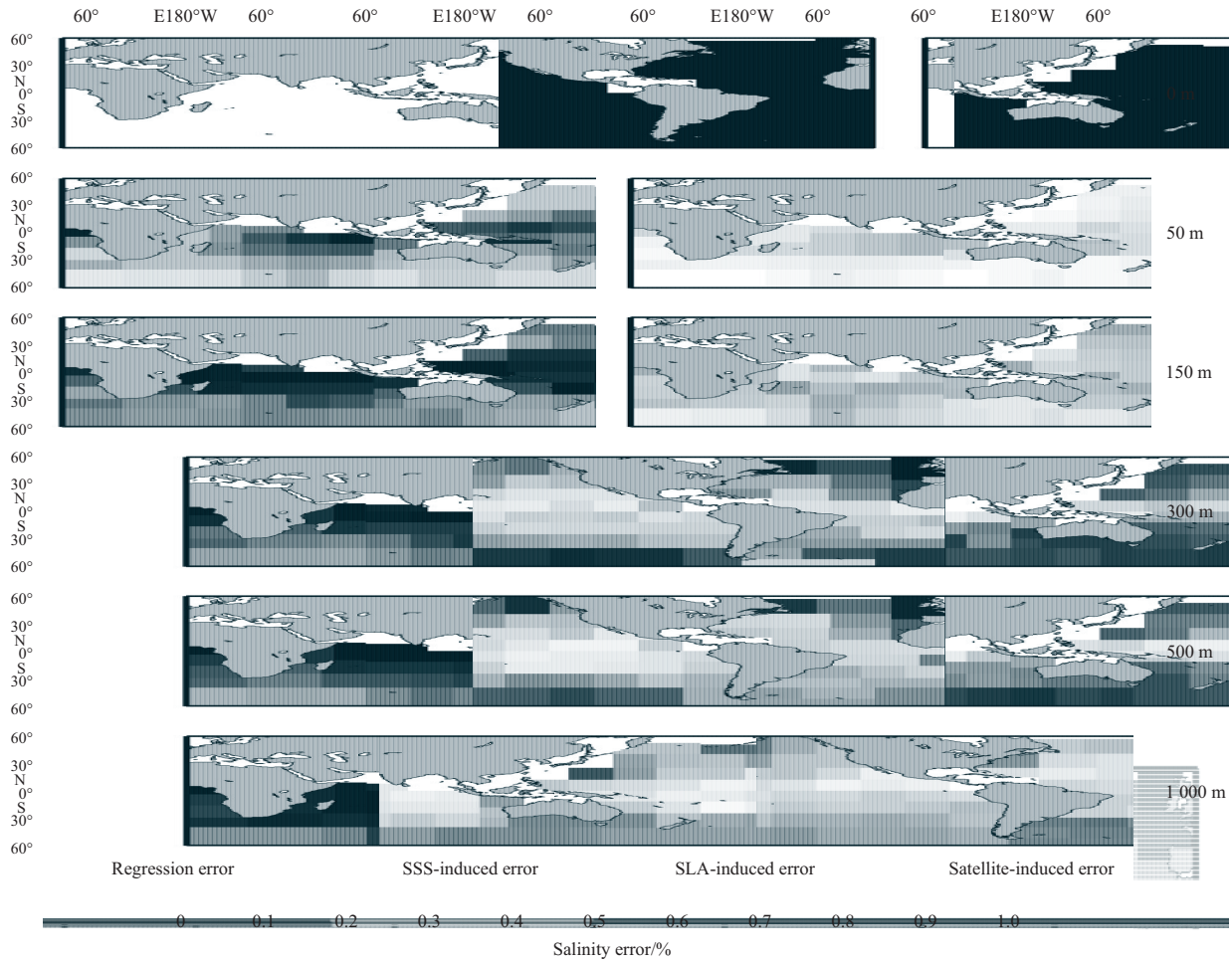

Fig. 8. Maps of p_{situ}, p_{satS}, p_{satH}, and p_{satSH} (from left to right) at depths of 0, 50, 150, 300, 500, and 1 000 m (from top to bottom). The SSS data used are from BEC-L3.

all of the inputs display consistently smooth patterns despite their different surface structures, although the CATDS-0.25° pattern has few small-scale structures. Thus, the vertical projection in this region eliminates much of the small-scale surface structures.

Figure 10 shows the salinity gradients for the same basin and time period as in Fig. 9. The SSS gradients in the CATDS-0.25° contain considerable small-scale noise. The SSS gradients associated with the WPSF are clearest in the BEC-L3 and weakest in the BEC-L4. The SSS gradients in the CATDS-1.00°, the Aquarius-V2, and the Aquarius-CAP are not as clear because of their relatively coarse 1° grids compared with the 0.25° grid spacing of the BEC-L3. At 100 m, the salinity gradients are significantly decreased, in particular for the CATDS-0.25°, the BEC-L3, and the Aquarius-CAP. For example, the noisy appearance of the gradient is almost absent in the CATDS-0.25°.

Figure 11 shows the salinity gradients in the KE region of the North Pacific Ocean, which is a mid-latitude open sea in the Northern Hemisphere. The CATDS-0.25° fields are still dominated by the small-scale noise, and the BEC-L3 is dominated by mesoscale features. The BEC-L4 SSS gradients are again slightly attenuated. It appears that the BEC-L4 is excessively smoothed by the procedure. The SSS gradients in the CATDS-1° and the Aquarius-V2 are roughly consistent with those in the ARIVO in terms of the positions and gradient magnitudes of the frontal regions. The Aquarius-CAP has a somewhat noisy, artificial pattern with unreasonable along-track strips across the frontal regions. This is also evident in the tropics (Fig. 10) and is presumably due to the exclusive use of scatterometer observations (without NECP ancillary data), which are highly dependent on the sampling characteristics of the Aquarius, or the absence of the smoothing procedure. In contrast to the cases shown in Fig. 10, the vertical projection at 100 m consistently retains most of the surface structures. Additional analyses in the South Pacific Ocean resulted in analogous conclusions (not shown).

Figure 12 shows the salinity gradients off the west coast of the United States, where strong coastal upwelling occurs. The CATDS-0.25° shows very strong SSS gradients that are unreasonably noisy everywhere. In the other retrievals, the strong offshore SSS gradients are frontal regions associated with eddies and meanders of the California Current. The coastal gradients are moderate in the CATDS-1.00°. The BEC-L4 magnitudes are as strong as those of BEC-L3, implying that BEC-L4 did not greatly attenuate the signals in coastal regions. Although the coastal gradients are almost nonexistent in the Aquarius-V2, their range is most similar to that of the ARIVO. In the Aquarius-CAP, the fields are also punctuated by swath-like noise. The retrieval method projects most of the surface gradients down to 100 m but weakens some possibly because the water is shallow near the shore.

To determine if the features described above are real signals or noise, a quantitative analysis of the spatial scales that these

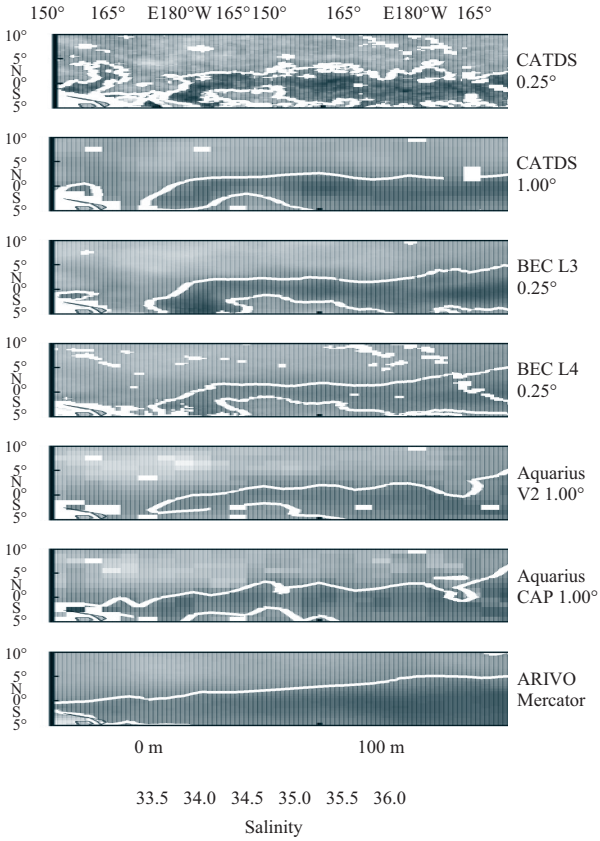

Fig. 9. The SSS (left) and retrieved salinity (right) at 100 m derived from the monthly CATDS-0.25°, CATDS-1.00°, BEC-L3, BEC-L4, Aquarius-V2, Aquarius-CAP, and ARIVO products (top to bottom) in the western Tropical Pacific Ocean (5°S–10°N, 150°E–160°W) for May 2012. The bold white lines are the 34.8 isohalines.

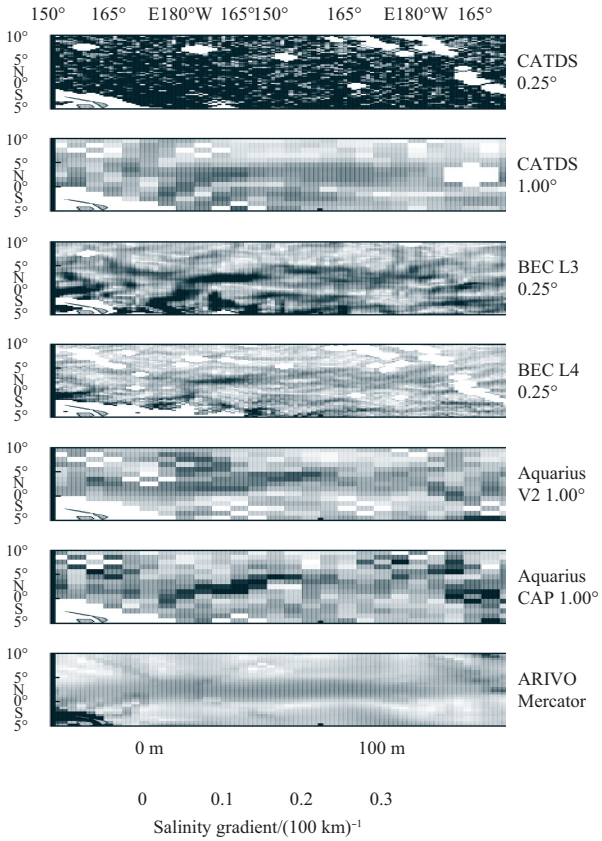

Fig. 10. Same as Fig. 9 but for the gradients of the salinity fields.

SSS retrievals can effectively resolve is required. The results show the zonal wave number spectra (Reynolds and Chelton, 2010) of the six retrievals: three open areas in the Pacific Ocean (Fig. 13) and three in the Atlantic Ocean (Fig. 14). The vertical projection affects the spectra energy contents at depth in very different ways in the tropics and extratropics. In most of the retrievals, the projection significantly decreases the energy in the spatial frequency higher than 10^{-1} $(°)^{-1}$ by an average of an order of magnitude in the tropics, while it retains nearly the same energy down to 100 m in the mid-latitude regions. This is consistent with the qualitative maps.

A consistent feature in all six panels of Figs 13 and 14 is that the CATDS-0.25° fields both on the surface and at 100 m have much higher spectral energy than any of the other five fields at wavelengths shorter than approximately 500 km (in the Pacific) or 300 km (in the Atlantic). In most cases, the spectra roll off of the CATDS-0.25° with a zonal wave number k is approximately k^{-2}. In contrast, the wave number dependences of the BEC-L3 and BEC-L4 spectra range from k^{-3} to k^{-4}. The CATDS-1.00°, Aquarius-V2, and Aquarius-CAP spectra are even shorter and steeper. On average, the spectral energy of the CATDS-0.25° is more than one order (the Northern Hemisphere) or two orders (the Southern Hemisphere) of magnitude higher than the other retrievals at the highest wave numbers. In the tropics, although the retrieved salinity fields at 100 m exhibit significantly weakened spectral energy for the CATDS-0.25° and other retrievals, the differences between them are still up to one order of magnitude. The existence of a k^{-2} spectrum is not generally an indication of data noise. However, the fundamentally different spectral behavior of the CATDS-0.25° fields compared with the other retrievals and the noisy, "speckled" appearance of the CATDS-0.25° fields in Figs 9–12 are clear indications that the CATDS-0.25° fields are dominated by the small-scale noise.

Another consistent feature is that the Aquarius-CAP SSS fields have significantly higher spectral energy than the Aquarius-V2 and CATDS-1° fields below approximately 300 km and down to the Nyquist frequency (100 km). The higher energy in the Aquarius-CAP at these scales might be an indication of noise, as is visible from the swath-like patterns in Figs 10 and 11. The lower energy level in the Aquarius-V2 is definitely caused by the smoothing procedure, which eliminated the swath patterns because the nonsmoothed Aquarius-V2 (not shown) has almost the same spectral energy as the Aquarius-CAP. The low spectral energy in the CATDS-1.00° SSS fields indicates that the CATDS procedure attenuates energy at these scales. At 100 m, the spectrum difference at the shortest wavelengths between the three 1.00°-resolution retrievals is almost absent after the vertical projection in the tropical and northern oceans and is moderately weakened in the southern oceans.

The differences between the BEC-L3 and the BEC-L4 are not surprising. On the surface, the BEC-L4 spectral energy at higher wave numbers, in particular at characteristic lengths between 100 and 25 km, is significantly less than the spectral energy of the BEC-L3 in the southern regions and slightly less in the tropical and northern regions. This is consistent with the attenuated ap-

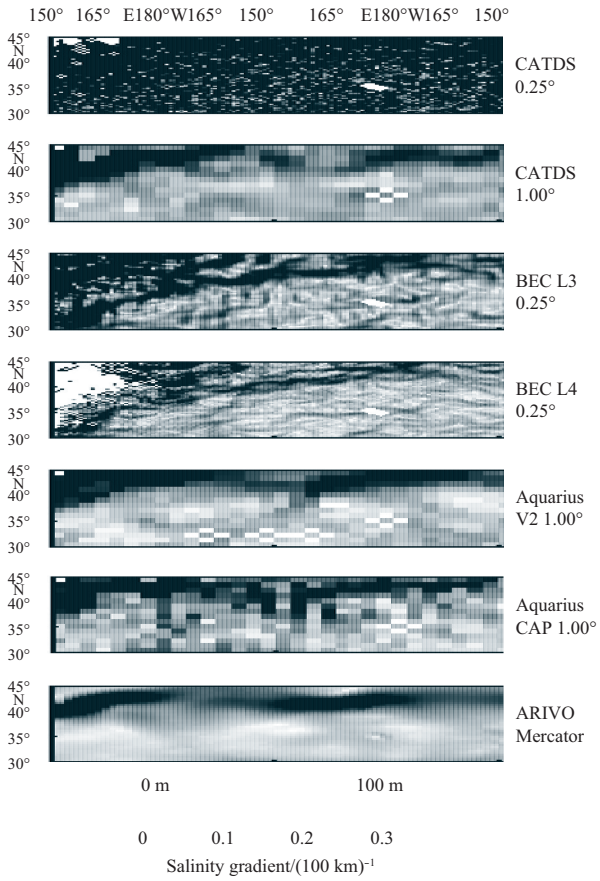

Fig. 11. Same as Fig. 10 but in the KE region (30°–45°N, 150°E–150°W).

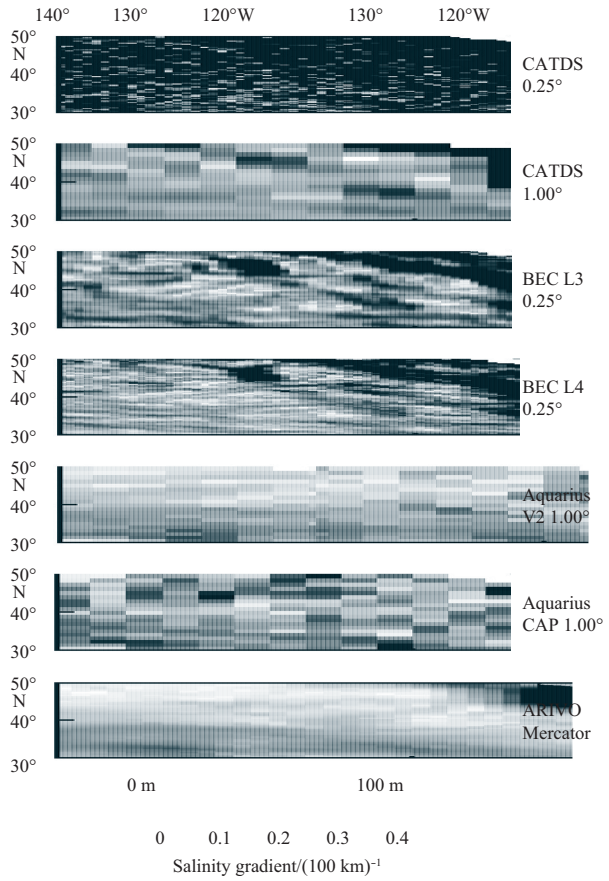

Fig. 12. Same as Fig. 10 but off the west coast of the United States (30°–50°N, 140°–110°W).

pearance of the BEC-L4 SSS shown in Fig. 9. Although the differences are not large, BEC-L4 has less mesoscale energy than the BEC-L3. This is likely attributable to the use of the SST template in the singularity analysis for the BEC-L4, which potentially attenuated the SSS fields. However, at 100 m, this difference is significantly reduced by the vertical projection except in the southern oceans, where the difference is much larger. Even if some of the energy of the BEC-L3 is considered to be noise, most are clearly related to mesoscale physical signals; this is indicated by the small RMS errors in Figs 2 and 4 and the reasonable appearances in Figs 9–12.

5 Discussion and conclusions

Several SSS retrievals were used to retrieve synthetic 3-D salinity fields from available satellite data. These SSS inputs were shown to work differently at different depths and in different regions.

In the mixed layer, the retrieved salinity is mainly influenced by the SSS information in several ways. (1) The spatial resolution, along with the temporal resolution to a looser extent, was shown to have an important influence on the SSS and the retrieved salinity within this layer because the SSS inputs perform better at the global scale as the spatial resolution decreases from 0.25° to 0.50° to 1.00°, or as the temporal resolution decreases from 10 days to monthly. That is because, a filtering or smoothing process, like the simple average implemented in SMOS-CATDS L3 products, is usually a trade off between the reduction of analysis error for the resolved low spatial frequency part of the spectrum and the loss of the variance associated with the filtered high spatial frequency part of the spectrum (Jordà and Gomis, 2010). In the SMOS, for example, the brightness temperature at L1 is reconstructed with a spatial resolution of 43 km. At L2, the brightness temperature data are transformed into the SSS on an approximately 15 km resolution grid due to the repetition cycle of the sampling. At L3, owning to the high observational noises in L1 or L2 data, the accuracy of SSS products may be not satisfactory unless we filter out part of the scales that can, in principle, be resolved by the satellite sampling. The result of filtering is an analysis of lower spatial resolution (e.g., 100 km) with a lower error, in which nevertheless the variance associated with short scales (e.g., 15 km) is lost. In other words, to measure the improvement from the averaging process, the analysis should be compared not with the "truth", but with the filtered "truth". In our case, the filtered "truth" is the SSS from the Argo network, which has a nominal resolution of approximately 300 km. Thus, on the premise that the SMOS has a much smaller ($\leqslant$43 km) nominal sampling, the products with lower spatial frequency (e.g., 1.00°) can be more accurate than those with relatively high spatial frequency (e.g., 0.50°, 0.25°), as it loses more higher spatial frequency part of the spectrum (e.g., the Rossby deformation radius on the order of 25 km or smaller). The same theory applies for the temporal resolution and Aquarius issues. (2) The projected SSS errors are generally dominant. With high and low accuracy SSS inputs in the tropics and extratropics, respectively, the estimates of salinity are more precise than climatology in the tropics but not in the extratropics. This is determined by the fewer number

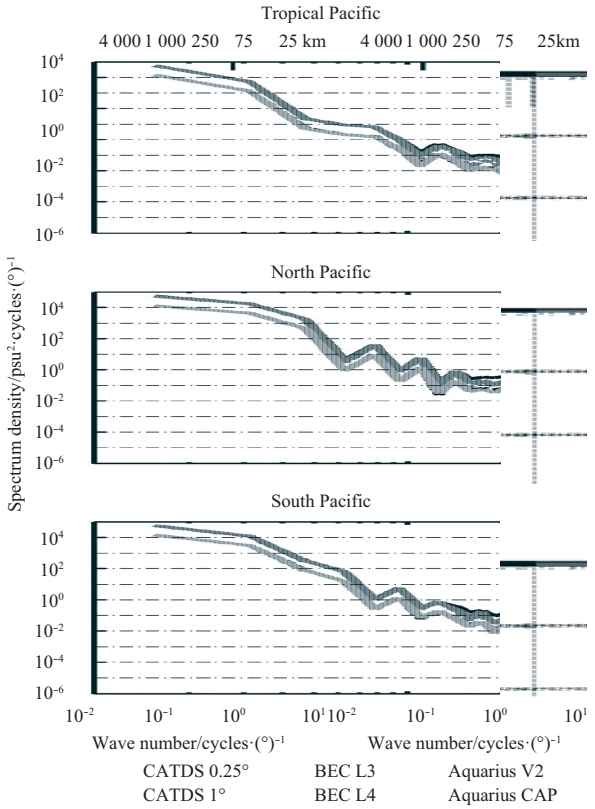

Fig. 13. Zonal wave number spectra computed from the SSS (left) and retrieved salinity at 100 m (right) for three open regions in the Pacific Ocean: the Tropical Pacific Ocean (5°S–10°N, 165°E–105°W; top), the North Pacific Ocean (30°–45°N, 160°E–135°W; middle), and the south Pacific Ocean (45°–30°S, 165°–90°W; bottom). For each region, the wave number spectra were computed from monthly salinity fields for all months of 2012 along each latitude of grid points within the specified domain; these individual spectra were then ensemble averaged over the latitudes and 12 months.

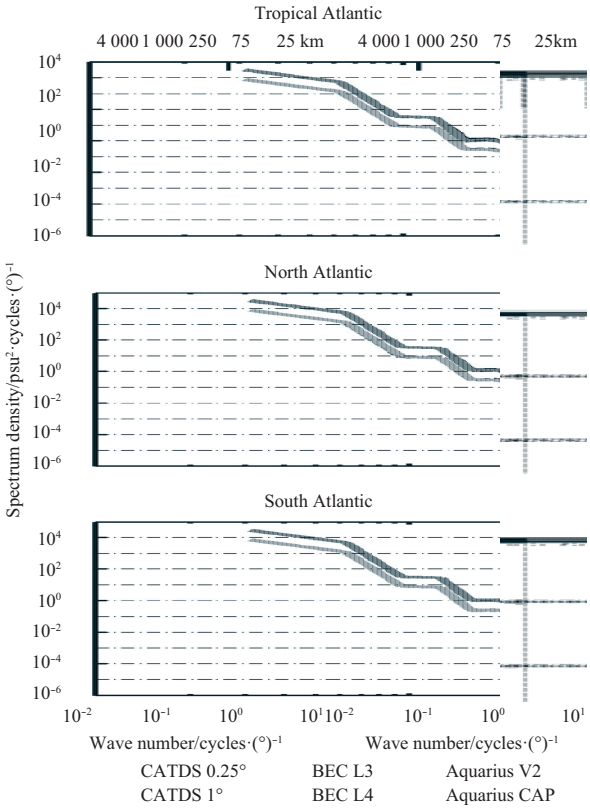

Fig. 14. Same as Fig. 13 but for three open regions in the Atlantic Ocean: the Tropical Atlantic Ocean (15°–5°S, 33°W–7°E; top), the North Atlantic Ocean (30°–40°N, 55°–15°W; middle), and the South Atlantic Ocean (45°–35°S, 45°–5°W; bottom).

of the brightness temperature data and lower sensitivity of dT_b/dS_{SS} to the SST at middle and high latitudes than in the tropics (Kerr et al., 2010). However, the regression errors dominate in certain tropical regions, such as the tropical Atlantic, where the anomalously large regression errors lead to salinity estimates with worse performance than the climatology. (3) Because the mixed layer is generally shallower in the tropics than in the extratropics, the mesoscale features and spectra energy of the SSS fields are greatly reduced at 100 m in the tropics but are mostly retained in the extratropics. Because the depth of the mixed layer varies by season, the manner in which the surface features are projected downward also varies by season.

Below the mixed layer, the retrieved S is mainly influenced by the SLA information. The regression errors gradually dominate and extend from the tropics to the extratropics. The displacement of the high-accuracy retrieved salinity fields to certain mid- and high-latitude regions (specifically the Northwest Pacific Ocean, the southwestern Tropical Pacific Ocean, the North and South Atlantic Ocean, and the Indian Ocean) reflects the higher SLA-S regression coefficients there, although the SLA errors (with respect to GPA) are also greater at higher latitudes (Guinehut et al., 2006). In contrast, the SSS-S regression coefficients are negligible and lead to the nonexistent SSS error patterns. An exception is the high-latitude southern oceans, where the maximum SSS-S regression coefficients propagate the maximum SSS errors down to the deep ocean.

Thus, the results can be summarized as follows. In the mixed layer, the accuracy of the retrieved salinity is roughly determined by the SSS accuracy in spite of the regression error pattern (except in the tropical Atlantic Ocean, where the regression errors are large). Below the mixed layer, the accuracy of the retrieved salinity is roughly determined by the magnitudes of the SLA-S regression coefficients in spite of the surface error (mainly from the SLA) pattern (except in the high-latitude southern oceans, where the SSS-induced errors are large). So, on the premise the regression coefficients cannot be changed (determined by the physical properties of the ocean), the current top priority is to improve the SSS observations especially at middle and high latitudes, where the SSS data are more prone to errors.

Different retrievals are compared in terms of the vertical errors, qualitative maps, and wave number spectra. (1) The CATDS-0.25° has larger RMS errors (w.r.t. Argo) and much more high-frequency energy which is associated with noise, and thus cannot be used with confidence. In contrast, CATDS-1.00° performs well throughout the tropics and has much lower noise energy at large scales. As illustrated above, it is because the average with larger filtering scales can reduce more noises related to small scales. (2) The Aquarius-CAP yields the lowest RMS errors because of the CAP algorithm, as claimed by previous studies (Reagan et al., 2014; Yueh et al., 2014). Nevertheless, its artificial appearance and greater high-frequency energy suggest that it may perform worse in depicting physical phenomena. In con-

trast, Aquarius-V2 has a more reasonable appearance and lower energy, which indicates that the smoothing procedure produces more physically based salinity fields at the cost of slightly increasing the RMS error. However, the relatively coarse 1.00° grids of the Aquarius-V2 and the Aquarius-CAP limit their feature resolutions only at large scales. (3) The visually attenuated appearance and flat spectra response at high frequencies for the BEC-L4 strongly suggest that the singularity analysis smoothes the SSS fields too much. This can be explained by the singularity exponents that are estimated from the high-quality SST, which reduce the effects of noise and artifacts on the SSS fields. In contrast, the smaller RMS errors, better performance than climatology for most of the tropical oceans, dominant mesoscale signals, and higher energy at short wave numbers of the BEC-L3 indicate that it may best represent the mesoscale phenomena in the SSS and 3-D salinity fields. This is consistent with previous studies including Hernandez et al. (2014) who showed the advantage of the SMOS over the Aquarius to reproduce SSS mesoscale features.

Therefore, to greatly improve the estimates of vertical salinity structures, especially in the extratropics and at mesoscale, some combined measures should be taken. It includes taking advantage of both the high resolution the with wide coverage of the SMOS and the high radiometric sensitivity of Aquarius, using more advanced algorithms (e.g., CAP) as useful supplement to the standard version, making a compromise between the low RMS error and high resolution, selecting the SSS retrievals with appropriate resolutions for specific physical phenomena, and so on.

References

Agarwal N, Sharma R, Basu S, et al. 2007. Derivation of salinity profiles in the Indian Ocean from satellite surface observations. IEEE Geoscience and Remote Sensing Letters, 4(2): 322–325

Ando K, McPhaden M J. 1997. Variability of surface layer hydrography in the tropical Pacific Ocean. Journal of Geophysical Research: Oceans (1978–2012), 102(C10): 23063–23078

Asher W E, Jessup A T, Branch R, et al. 2014. Observations of rain-induced near-surface salinity anomalies. Journal of Geophysical Research: Oceans (1978–2012), 119(8): 5483–5500

Ballabrera-Poy J, Mourre B, Garcia-Ladona E, et al. 2009. Linear and non-linear *T*-*S* models for the eastern North Atlantic from Argo data: role of surface salinity observations. Deep-Sea Research: Part I. Oceanographic Research Papers, 56(10): 1605–1614

Boutin J, Martin N, Reverdin G, et al. 2014. Sea surface salinity under rain cells: SMOS satellite and *in situ* drifters observations. Journal of Geophysical Research: Oceans (1978–2012), 119(8): 5533–5545

Buongiorno Nardelli B. 2012. A novel approach for the high-resolution interpolation of *in situ* sea surface salinity. Journal of Atmospheric and Oceanic Technology, 29(6): 867–879

Buongiorno Nardelli B. 2013. Vortex waves and vertical motion in a mesoscale cyclonic eddy. Journal of Geophysical Research: Oceans (1978–2012), 118(10): 5609–5624

Buongiorno Nardelli B, Guinehut S, Pascual A, et al. 2012. Towards high resolution mapping of 3-D mesoscale dynamics from observations. Ocean Science, 8(5): 885–901

Buongiorno Nardelli B, Santoleri R. 2004. Reconstructing synthetic profiles from surface data. Journal of Atmospheric and Oceanic Technology, 21(4): 693–703

Buongiorno Nardelli B, Santoleri R. 2005. Methods for the reconstruction of vertical profiles from surface data: multivariate analyses, residual GEM, and variable temporal signals in the North Pacific Ocean. Journal of Atmospheric and Oceanic Technology, 22(11): 1762–1781

Carnes M R, Teague W J, Mitchell J L. 1994. Inference of subsurface thermohaline structure from fields measurable by satellite. Journal of Atmospheric and Oceanic Technology, 11(2): 551–566

Delcroix T, Hénin C, Porte V, et al. 1996. Precipitation and sea-surface salinity in the tropical Pacific Ocean. Deep-Sea Research: Part I. Oceanographic Research Papers, 43(7): 1123–1141

Dinnat E P, Boutin J, Yin Xiaobin, et al. 2014. Inter-comparison of SMOS and Aquarius sea surface salinity: effects of the dielectric constant and vicarious calibration. In: Proceedings of the 13th Specialist Meeting on Microwave Radiometry and Remote Sensing of the Environment. Pasadena, CA: IEEE, 55–60

Drucker R, Riser S C. 2014. Validation of Aquarius sea surface salinity with Argo: analysis of error due to depth of measurement and vertical salinity stratification. Journal of Geophysical Research: Oceans (1978–2012), 119(7): 4626–4637

Font J, Boutin J, Reul N, et al. 2010. Overview of SMOS level 2 ocean salinity processing and first results. In: Proceedings of IEEE International Geoscience and Remote Sensing Symposium (IGARSS). Honolulu, HI: IEEE, 3146–3149

Fox D N, Teague W J, Barron C N, et al. 2002. The modular ocean data assimilation system (MODAS). Journal of Atmospheric and Oceanic Technology, 19(2): 240–252

Guimbard S, Gourrion J, Portabella M, et al. 2012. SMOS semi-empirical ocean forward model adjustment. IEEE Transactions on Geoscience and Remote Sensing, 50(5): 1676–1687

Guinehut S, Dhomps A L, Larnicol G, et al. 2012. High Resolution 3-D temperature and salinity fields derived from *in situ* and satellite observations. Ocean Science Discussions, 9(2): 1313–1347

Guinehut S, Le Traon P Y, Larnicol G. 2006. What can we learn from Global Altimetry/Hydrography comparisons?. Geophysical Research Letters, 33(10): L10604

Guinehut S, Le Traon P Y, Larnicol G, et al. 2004. Combining Argo and remote-sensing data to estimate the ocean three-dimensional temperature fields—A first approach based on simulated observations. Journal of Marine Systems, 46(1–4): 85–98

Hernandez O, Boutin J, Kolodziejczyk N, et al. 2014. SMOS salinity in the subtropical North Atlantic salinity maximum: 1. Comparison with Aquarius and *in situ* salinity. Journal of Geophysical Research: Oceans (1978–2012), 119(12): 8878–8896

Johnson J T, Zhang Min. 1999. Theoretical study of the small slope approximation for ocean polarimetric thermal emission. IEEE Transactions on Geoscience and Remote Sensing, 37(5): 2305–2316

Jordà G, Gomis D. 2010. Accuracy of SMOS level 3 SSS products related to observational errors. IEEE Transactions on Geoscience and Remote Sensing, 48(4): 1694–1701

Kerr Y H, Waldteufel P, Wigneron J P, et al. 2010. The SMOS mission: new tool for monitoring key elements of the global water cycle. Proceedings of the IEEE, 98(5): 666–687

Larnicol G, Guinehut S, Rio M H, et al. 2006. The global observed ocean products of the French Mercator project. In: Proceedings of the Symposium on 15 Years of progress in radar altimetry. Noordwijk, Netherlands: ESA Special Publication

Le Vine D M, Lagerloef G S E, Torrusio S E. 2010. Aquarius and remote sensing of sea surface salinity from space. Proceedings of the IEEE, 98(5): 688–703

Maes C, Behringer D. 2000. Using satellite-derived sea level and temperature profiles for determining the salinity variability: a new approach. Journal of Geophysical Research: Oceans (1978–2012), 105(C4): 8537–8547

Meinen C S, Watts D R. 2000. Vertical structure and transport on a transect across the North Atlantic Current near 42°N: time series and mean. Journal of Geophysical Research: Oceans (1978–2012), 105(C9): 21869–21891

Meissner T, Wentz F J. 2012. The emissivity of the ocean surface between 6 and 90 GHz over a large range of wind speeds and earth incidence angles. IEEE Transactions on Geoscience and Remote Sensing, 50(8): 3004–3026

Meissner T, Wentz F, Hilburn K, et al. 2012. The Aquarius salinity retrieval algorithm. In: Proceedings of IEEE International Geoscience and Remote Sensing Symposium. Munich: IEEE

Meissner, T, Wentz F, Ricciardulli L. 2014. The emission and scattering of L-band microwave radiation from rough ocean surfaces

and wind speed measurements from the Aquarius sensor. Journal of Geophysical Research: Oceans (1978–2012), 119(9): 6499–6522

Mitchell D A, Wimbush M, Watts D R, et al. 2004. The residual GEM technique and its application to the southwestern Japan/East Sea. Journal of Atmospheric and Oceanic Technology, 21(12): 1895–1909

Mulet S, Rio M H, Mignot A, et al. 2012. A new estimate of the global 3D geostrophic ocean circulation based on satellite data and in-situ measurements. Deep-Sea Research: Part II. Topical Studies in Oceanography, 77–80: 70–81

Ohno Y, Kobayashi T, Iwasaka N, et al. 2004. The mixed layer depth in the North Pacific as detected by the Argo floats. Geophysical Research Letters, 31(11): L11306

Pablos M, Piles M, González-Gambau V, et al. 2014. SMOS and Aquarius radiometers: inter-comparison over selected targets. IEEE Journal of Selected Topics in Applied Earth Observations and Remote Sensing, 7(9): 3833–3844

Reagan J, Boyer T, Antonov J, et al. 2014. Comparison analysis between Aquarius sea surface salinity and World Ocean Database *in situ* analyzed sea surface salinity. Journal of Geophysical Research: Oceans (1978–2012), 119(11): 8122–8140

Reynolds R W, Chelton D B. 2010. Comparisons of daily sea surface temperature analyses for 2007–08. Journal of Climate, 23(13): 3545–3562

Telszewski M, Chazottes A, Schuster U, et al. 2009. Estimating the monthly pCO_2 distribution in the North Atlantic using a self-organizing neural network. Biogeosciences Discussions, 6(2): 3373–3414

Turiel A, Nieves V, García-Ladona E, et al. 2009. The multifractal structure of satellite sea surface temperature maps can be used to obtain global maps of streamlines. Ocean Science, 5(4): 447–460

Wu Xiangbai, Yan Xiaohai, Jo Y H, et al. 2012. Estimation of subsurface temperature anomaly in the North Atlantic using a self-organizing map neural network. Journal of Atmospheric and Oceanic Technology, 29(11): 1675–1688

Xie P, Boyer T, Bayler E, et al. 2014. An *in situ*-satellite blended analysis of global sea surface salinity. Journal of Geophysical Research: Oceans (1978–2012), 119(9): 6140–6160

Yueh S H, Chaubell J. 2012. Sea surface salinity and wind retrieval using combined passive and active L-band microwave observations. IEEE Transactions on Geoscience and Remote Sensing, 50(4): 1022–1032

Yueh S, Tang Wenqing, Fore A, et al. 2014. Aquarius geophysical model function and combined active passive algorithm for ocean surface salinity and wind retrieval. Journal of Geophysical Research: Oceans (1978–2012), 119(8): 5360–5379